Symmetry reduction in the electronic structure of heavily overdoped Pb-Bi2201 detected by ARPES

Y. Miyai[a], T. Kurosawa[b], M. Oda[c], M. Arita[d], S. Ideta[d], and K. Shimada[d]

[a]*Graduate School of Science, Hiroshima University, Kagamiyama 1-3-1, Higashi-Hiroshima 739-8526, Japan*
[b] *Fuculty of Science and Engineearing, Muroran Institute of Technology, 27-1 Mizumoto-cho, Muroran, Hokkaido, 050-8585, Japan*
[c] *Department of Physics, Hokkaido University, Sapporo 060-0809, Japan*
[d] *Hiroshima Synchrotron Radiation Center, Hiroshima University, Kagamiyama 1-3-1, Higashi-Hiroshima 739-8526, Japan*

Keywords: High-T_C superconductor, ARPES

High transition-temperature (T_C) cuprate superconductors have attracted much interest since their discovery in 1986 for their high superconducting transition temperature as well as unusual physical properties such as a pseudogap state and a nematic phase [1,2]. Superconductivity occurs in the CuO_2 plane and the Cu $3d_{x^2-y^2}$ state forms the Fermi surface. One can expect a four-fold symmetry of the Fermi surface because the CuO_2 plane is tetragonal. However, symmetry reduction of the electronic structure has been reported in Bi-based cuprate superconductors recently [2,3]. Similar symmetry reduction or *nematicity* was found in the Fe-based superconductor, the electronic states break the four-fold rotational symmetry of the lattice [4]. Although nematicity in electron liquids has attracted much interest, the rotational symmetry breaking in the electronic states for high-T_C cuprate superconductors has not been clarified yet.

Here, we have examined the symmetry of the electronic structure of heavily overdoped $(Bi,Pb)_2Sr_2CuO_{6+\delta}$ (Pb-Bi2201) (T_C = 6 K) using high-resolution angle-resolved photoemission spectroscopy (ARPES). We selected Bi2201 because it has a single CuO_2 plane and one can exclude the complexity of the electronic structure such as bilayer splitting derived from plural CuO_2 planes. Furthermore, the heavily overdoped sample is favorable because the pseudogap is vanishing and one can clearly detect the Fermi surface in the normal state.

Figures 1(a) and (b) show the Fermi surface measured at $h\nu$ = 22 eV, *s*-polarization, and T = 20 K along two orthogonal nodal directions. We found a clear difference in the nodal distances; $d_1 = (7.948 \pm 0.003) \times 10^{-1}$ Å^{-1} (Fig. 1(a)) and $d_2 = (8.340 \pm 0.003) \times 10^{-1}$ Å^{-1} (Fig. 1(b)). These distances are temperature independent for the temperature range from T = 20 K up to 260 K (Fig. 1(c)). In addition, we have conducted MDC analysis along these two nodal directions and find different quasiparticle lifetime broadening as shown in Fig. 1(d), which is persistent up to 260 K. The situation is similar for the samples with T_C = 4, 6, and 10 K. Our results indicate the reduction of the four-fold symmetry in the electronic states.

In the heavily overdoped region, a charge density wave (CDW) is observed by resonant inelastic X-ray scattering and its onset is well above 250 K [5]. In addition, previous Raman scattering measurements suggest the Pomeranchuk instability and the nematic phase [6]. The previous reports are in line with our findings. Further study is required to reveal how symmetry reduction in the electronic state occurs in the heavily overdoped region. To investigate this issue, we are planning to examine the electronic structure at the endpoint of the hole concentration in the pseudogap state and at the onset of the Lifshitz transition that occurs between the hole-like and electron-like Fermi surfaces.

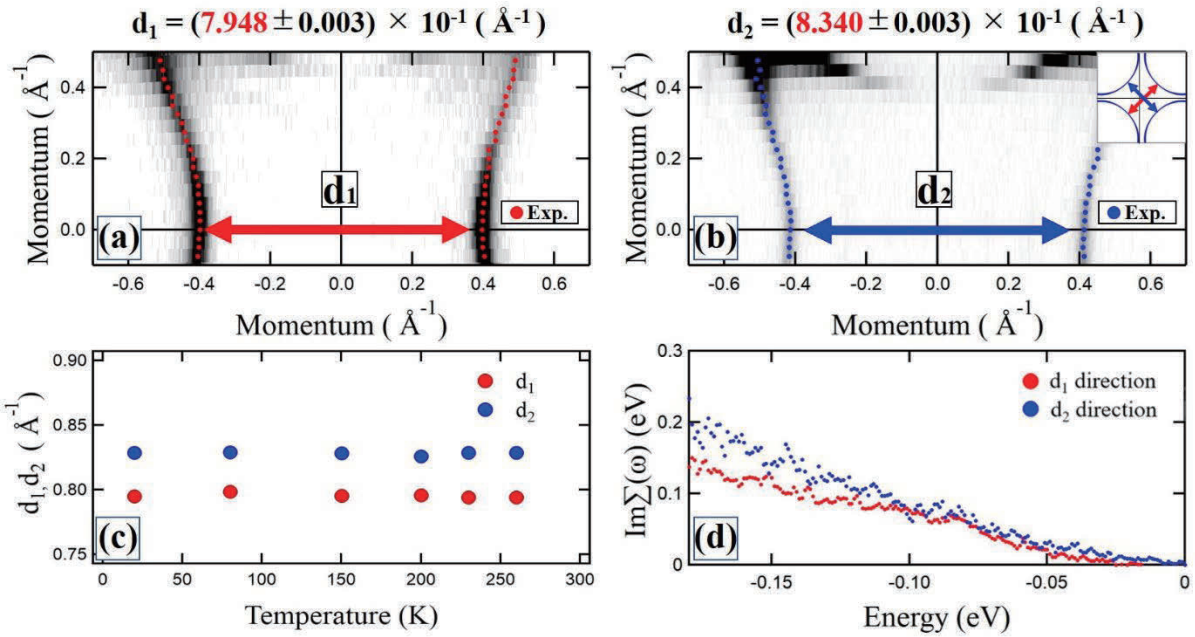

FIGURE 1. (a), (b) Fermi surface observed at $h\nu = 22$ eV, *s*-polarization and $T = 20$ K along the nodal directions shown in the inset of panel (b). The inset displays the Fermi surface centered at the $\bar{\Gamma}$ point. Red and blue dots indicate the Fermi surface points determined from the peaks of the momentum distribution curves. d_1 and d_2 indicate the distance between nodes. (c) Temperature dependence of d_1, d_2. (d) $Im\Sigma$ of the self-energy along d_1 and d_2 nodal directions.

1. M. Hashimoto *et al*., *Nature Physics* **10**, 483-495 (2014).
2. S. Nakata *et al*., *npj Quantum Materials* **6**, 86 (2021).
3. Y. He *et al*., *Scientific Reports* **7**, 8059 (2017).
4. H. C. Xu *et al*., *Physical Review Letters* **117**, 157003 (2016).
5. Y. Y. Peng *et al*., *Nature Materials* **17**, 697 (2018).
6. N. Auvray *et al., Nature Communications* **10**, 5209 (2019).

Re-examination of the phase diagram of the high-T_c cuprate superconductor $Bi_2Sr_2CaCu_2O_{8+\delta}$ studied by ARPES

Y. Tsubota[a], Y. Miyai[a], S. Nakagawa[e], S. Ishida[d], S. Kumar[b], K. Tanaka[c], H. Eisaki[d], T. Kashiwagi[e], M. Arita[b], K. Shimada[a,b], and S. Ideta[a,b]

[a] *Graduate School of Advanced Science and Engineering, Hiroshima Univ., Higashi-Hiroshima 739-0046, Japan*
[b] *Hiroshima Synchrotron Radiation Center (HiSOR), Hiroshima Univ., Higashi-Hiroshima 739-0046, Japan*
[c] *UVSOR-Ⅲ Synchrotron, Institute for Molecular Science, Okazaki, Aichi 444-8585, Japan*
[d] *National Institute of Advanced Industrial Science and Technology (AIST), Tsukuba, Ibaraki 305-8560, Japan*
[e] *Division of Materials Science, Tsukuba University, Tsukuba, Ibaraki 305-8577, Japan*

Keywords: high-T_c cuprate superconductors, ARPES, electronic structure, strongly correlated electron materials

It has been known that the cuprate superconductors show a high superconducting (SC) transition temperature (T_c) and exotic physical properties. However, the SC mechanism has been unclear yet. In order to understand the mechanism of high-T_c cuprates, $Bi_2Sr_2CaCu_2O_{8+\delta}$ (Bi2212) is one of the promising candidates to study the electronic structure and reveal the physical properties. Bi-based double-layer cuprate, Bi2212 has two CuO_2 planes in the unit cell and shows the high T_c around 95 K at the optimally doped sample. Carrier doping (hole/electron concentration) is an important key parameter in cuprates because superconductivity occurs upon hole doping in the CuO_2 plane and the amount of hole doping controls the T_c [1, 2]. The electronic phase diagram of hole-doped high-T_c cuprate superconductors plotted as a function of temperature and carrier concentration has been reported as an empirical and universal phase diagram, where the phase diagram is a dome-like shape centered at ~0.16 of hole concentration [1]. However, according to the previous ARPES studies, the empirical phase diagram would not be universal and might be shifted toward the overdoped region [2-4]. Therefore, in the present study, we have performed an angle-resolved photoemission spectroscopy (ARPES) measurements to study whether the phase diagram changes depending on sample compositions or not.

In this study, we have systematically performed ARPES measurements to directly investigate the electronic structure of the underdoped, optimally doped, and overdoped Bi2212. ARPES experiments were carried out at BL-9A. We measured several samples in the SC and normal states with different hole concentration and compositions: underdoped $Bi_{2.1}Sr_{1.9}CaCu_2O_{8+\delta}$ (T_c ~ 75 K)(Bi2.1-UD75), underdoped $Bi_{2.3}Sr_{1.7}CaCu_2O_{8+\delta}$ (T_c ~ 70 K)(Bi2.3-UD70), optimally doped $Bi_{2.1}Sr_{1.9}CaCu_2O_{8+\delta}$ (T_c ~ 92 K)(Bi2.1-Opt92), optimally doped $Bi_{2.3}Sr_{1.7}CaCu_2O_{8+\delta}$ (T_c ~ 85 K)(Bi2.3-Opt85), optimally doped $Bi_{2.1-x}Pb_xSr_2CaCu_2O_{8+\delta}$ (x = 0.66, T_c ~ 97 K)(Pb-Opt97) and overdoped $Bi_{2.1}Sr_{1.9}CaCu_2O_{8+\delta}$ (T_c ~ 76 K)(Bi2.1-OD74, Bi2.1-OD76). High quality single crystals of Bi2212 were cleaved *in-situ* in the ultrahigh vacuum of ~5×10^{-9} Pa.

Figure 1 (a) shows the momentum dependence of the Fermi momentum (k_F) estimated from the momentum distribution curve (MDC) ($h\nu$ = 17.8 eV and T = 30 K). In addition, the data that we have obtained from the optimally doped samples in the present study are plotted. Around the nodal region, the k_F is defined at Fermi level (E_F) by single Lorentzian. On the other hand, from the off-nodal to the anti-nodal region, the k_F is defined at the momentum which shows the gap minimum by fitting with double Lorentzian. We have determined hole concentration from the Fermi surface area quantitatively and compared them as shown in Fig. 1 (b), which indicate the new phase diagram in the ARPES study. As a result, we have found that the phase diagram (Fig. 1 (b)) is different from the previous empirical phase diagram which was reported by Tallon *et al* [1]. We have figured out that the phase diagram changes depending on sample compositions. As a future work, we continue to study the electric structure of underdoped and overdoped samples to make an entire phase diagram of Bi2212.

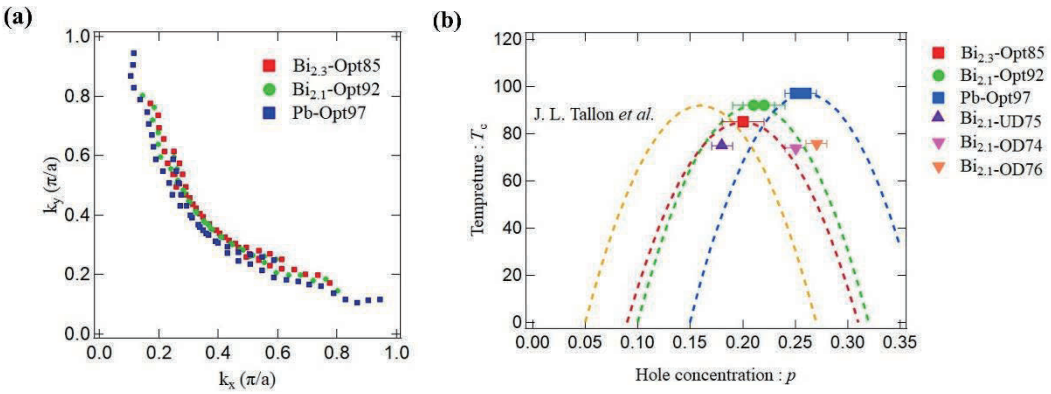

FIGURE 1. (a) Fermi momentum obtained from the optimally doped samples plotted in the k_x-k_y momentum space for Bi2212 (30 K). The shape of Fermi surface varies for each composition. (b) The new phase diagram of Bi2212 in the present ARPES study.

REFERENCES

1. J. L. Tallon, C. Bernhard, H. Shaked, R. L. Hitterman and J. D. Jorgensen, *Phys. Rev. B* **51**, 12911 (1995).
2. I. K. Drozdov, I. Pletikosić, C.-K. Kim, K. Fujita, G. D. Gu, J. C. Séamus Davis, P. D. Johnson1, I. Božović and T. Valla, *Nat. Commun*. **9**, 5210 (2018).
3. R. Sodota, N. Kudo, M. Matsunami, and T. Takeuchi, *J. Phys. Soc. Jpn.* **88**, 064711 (2019).
4. H. Sakamoto, K. Ogawa, T. Kondo, S. Shin, M Matsunami, H. Ikuta, and T. Takeuchi, *J. Phys. Soc. Jpn.* **85**, 104710 (2016).

Temperature-dependent Fermi surface evolution at the valence transition of $YbInCu_4$

Hiroaki Anzai[a], Atsushi Hariki[a], Hitoshi Sato[b], Masashi Arita[b], Tao, Zhuang[c], and Koichi Hiraoka[c]

[a] *Graduate School of Engineering, Osaka Prefecture University, Sakai 599-8531, Japan*
[b] *Hiroshima Synchrotron Radiation Center, Hiroshima University, Higashi-Hiroshima 739-0046, Japan*
[c] *Graduate School of Science and Engineering, Ehime University, Matsuyama 790-8577, Japan*

Keywords: *c-f* hybridization, Yb compound, photoemission spectroscopy.

The first-order valence transition is one of the most controversial topics in Yb-based compounds. In particular, the relationship between the first-order valence transition and the hybridization of the conduction electrons with the 4*f* electrons (*c-f* hybridization) has been discussed for a long time. For $YbInCu_4$, the Kondo temperature, which is a measure of the *c-f* hybridization strength, changes from $T_K \sim 25$ K in the high-temperature phase ($T > T_v = 42$ K) to $T_K \sim 400$ K in the low-temperature phase ($T < T_v$) [1,2]. The *f-f* interaction strength does not significantly depend on the perturbation. Thus, the experimental challenge of the mechanism for the valence transition lies in understanding the temperature-evolution of the *c-f* hybridization and the Fermi surface volume [3].

Here, we report angle-resolved photoemission spectroscopy measurements of $YbInCu_4$ [4]. The experiments were performed at BL-9A of Hiroshima Synchrotron Radiation Center. The samples were cleaved *in situ* along (111) crystal plane. The data were acquired with $h\nu = 24$ eV photons. The energy resolution was set to 17 meV.

Figure 1(a) shows the Fermi surface map at $T = 10$ K in the low-temperature phase. The elliptical shape of the intensity contours is observed around the Brillouin zone corner. In Fig. 1(b1)-1(b3), we show the ARPES spectra along three momentum directions, which are indicated by green curves in Fig. 1(a). The $4f_{7/2}$ states are observed as bright regions at $|\omega| \sim 0.04$ eV. A small, but finite, weight of the conduction band exists at $|\omega| < 0.03$ eV. This band reaches E_F and can be assigned to the electron band, as demonstrated by the peak positions of the momentum distribution curves (MDCs) in Figs. 1(b1)-1(b3) and 1(c). We determined the Fermi momentum k_F from the peak positions of the MDCs at E_F and plot them using open circles in Fig. 1(a). The electron band forms the elliptical Fermi pocket centered at the $\bar{\mathrm{M}}$ point.

The ARPES data at $T = 50$ K in the high-temperature phase are shown in Figs. 1(d)-1(f). The elliptical electron Fermi surface still exists around the $\bar{\mathrm{M}}$ point, as shown in Fig. 1(d). It should be noted that the Fermi momentum of the electron band shifts toward $k = 0$ Å^{-1}, causing a shrinkage of the Fermi surface above T_V. The peak positions of the MDCs at both $T = 10$ and 50 K in cut 3 are summarized in Fig. 1(g), revealing a rigid-band-like behavior of the electron band at T_V. For quantitative analysis, the MDC peak positions in the momentum direction of cut 3 are fitted by a quadratic dispersion of $a + b\omega^2$, and the results are plotted as dashed curves in Fig. 1(g). The parameters are set to $(a, b) = (-0.09, 2.7)$ and $(-0.06, 6.5)$ for the low- and high-temperature phases, respectively. The curvature of the band dispersion decreases below T_V along with the energy shift of 0.03 eV, implying a change in the strength of the hybridization between the $4f_{7/2}$ states and the conduction bands [3].

The ratio of the band velocities for the bare and renormalized electrons is an indicator of the correlation-induced enhancement of the effective mass [5]. We can extract a similar quantity, namely, the mass enhancement factor, from the ratio between the Fermi velocity in the high-temperature phase v_F^{HT}, which approximates the velocity with no *c-f* hybridization, and the hybridized Fermi velocity in the low-temperature phase v_F^{LT}. The two velocities are determined by differentiating the fitting data in Fig. 1(g). The mass enhancement factor of $v_F^{HT}/ v_F^{LT} = 1.33$ provides direct evidence of the increase in the hybridization strength below T_V.

Based on the identified band dispersion, we have estimated the area of the Fermi surface from Figs. 1(a) and 1(d). For a two-dimensional Fermi surface, the number of conduction electrons per unit cell n is given by the

Luttinger theorem as $n = A_{FS} / A_{BZ}$, where A_{FS} is the area of the Fermi surface and A_{BZ} is the area of the surface-projected Brillouin zone [6]. We found that the number n in the low- and high-temperature phases is $n_{LT} = 0.51$ and $n_{HT} = 0.33$ per surface unit cell of the $YbInCu_4$ (111) plane, respectively. The ratio of $n_{LT} / n_{HT} = 1.55$ demonstrates a reconstruction from a small to a large Fermi surface at T_V. The enhancement of the carrier mobility at E_F is in good agreement with the substantial reduction in the electrical resistivity below T_V. Our observations are consistently explained by the concept that the Kondo temperature and the Yb valence are associated with the position of the Fermi level relative to the quasigap, as demonstrated by open-core LDA calculations in Fig. 1(h) [7]. The enhancement in the density of states at E_F due to the *c-f* hybridization should be incorporated into scenarios of the first-order valence transition of $YbInCu_4$.

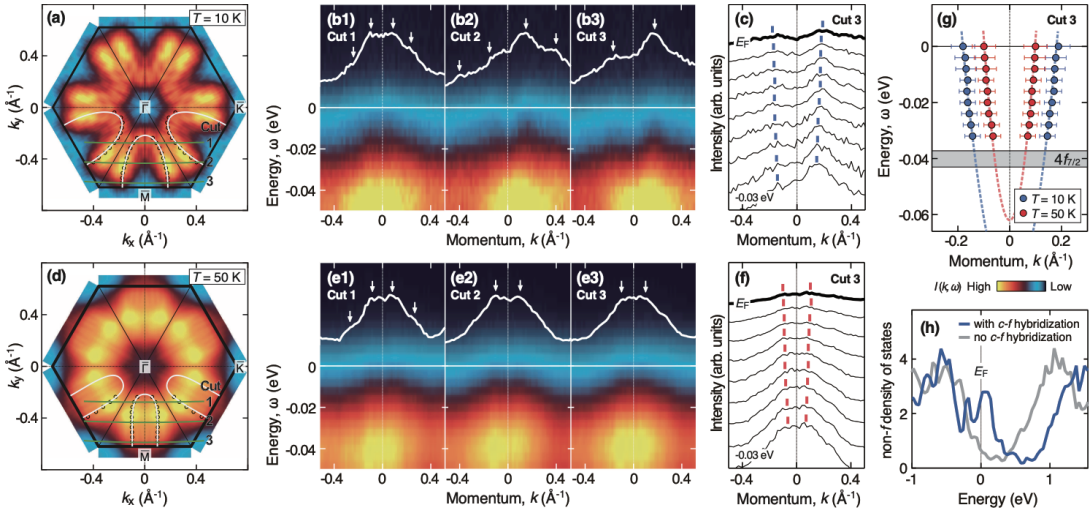

Figure 1. (a) Fermi surface map of $YbInCu_4$ at $T = 10$ K. The map is obtained by integrating the spectral intensity over an energy window of $|E_F| < 0.01$ eV and symmetrized by flipping and rotating the raw data along the high-symmetry lines. The black open circles represent the Fermi momentum k_F. The white outlines denote a Fermi surface constructed by tracking k_F. (b1)-(b3) Band dispersion at $T = 10$ K along three momentum cuts, as labeled in (a). The momentum distribution curves (MDCs) at E_F are also displayed as white curves. The arrows indicate the peak positions of the MDCs. (c) MDCs of the ARPES spectra along Cut 3 of (b3) in an energy range of $0 < |E_F| < 0.03$ eV. The blue bars indicate the peak positions. (d) Fermi surface map at $T = 50$ K. The integration energy window, the lines, and the marks are the same as those in (a). (e1)-(e3) Band dispersion at $T = 50$ K along three momentum cuts, as labeled in (d). (f) MDCs of the ARPES spectra at $T = 50$ K along Cut 3 of (e3). (g) Summary of the peak positions in (c) and (f). The blue and red circles are the peak positions of MDCs at $T = 10$ K and 50 K, respectively. The dashed curves are quadratic dispersions of $a + b\omega^2$. The fitting parameters are set to $(a, b) = (-0.09, 2.7)$ and $(-0.06, 6.5)$ at $T = 10$ K and 50 K, respectively. The gray shaded area represents the energy of the Yb^{2+} $4f_{7/2}$ states. (h) Comparison of the non-*f* density of states obtained by open-core LDA calculations. The blue and gray curves indicate the non-*f* density of states with *c-f* hybridization and no *c-f* hybridization, respectively.

REFERENCES

1. I. Felner, I. Nowik, D. Vaknin, U. Potzel, J. Moser, G. M. Kalvius, G. Wortmann, G. Schmiester, G. Hilscher, E. Grantz, C. Schmitzer, N. Pillmayr, K. G. Prasad, H. de Waard, and H. Pinto, Phys. Rev. B **35**, 6956 (1987).
2. J. L. Sarrao, C. D. Immer, C. L. Benton, Z. Fisk, J. M. Lawrence, D. Mandrus and J. D. Thompson, Phys. Rev. B **54**, 12207 (1996).
3. H. Anzai, S. Ishihara, K. Mimura, H. Sato, M. Arita, T. Zhuang, and K. Hiraoka, Phys. Rev. Res. **2**, 033408 (2020).
4. H. Anzai, A. Hariki, H. Sato, M. Arita, T. Zhuang, and K. Hiraoka, Phys. Rev. B **108**, 075116 (2023).
5. H. Anzai, A. Ino, T. Kamo, T. Fujita, M. Arita, H. Namatame, M. Taniguchi, A. Fujimori, Z.-X. Shen, M. Ishikado, and S. Uchida, Phys. Rev. Lett. **105**, 227002 (2010).
6. J. M. Luttinger, Phys. Rev. **119**, 1153 (1960).
7. E. Figueroa, J. M. Lawrence, J. L. Sarrao, Z. Fisk, M. F. Hundley, and J. D. Thompson, Solid State Commun. **106**, 347 (1998).

Direct Observation of Electronic Structure in Electron-doped ZrNCl by Synchrotron ARPES

N. Kataoka[a], R. Saitou[a], M. Tanaka[b], M. Arita[c], K. Shimada[c], T. Wakita[a, d] and T. Yokoya[a, d]

[a]*Graduate School of Natural Science and Technology, Okayama University, Japan*
[b]*Graduate School of Engineering, Kyushu Institute of Technology, Japan*
[c]*Hiroshima Synchrotron Radiation Center, Hiroshima University, Japan*
[d]*Research Institute for Interdisciplinary Science, Okayama University, Japan*

Keywords: Layered Nitride Chloride, ARPES

Layered nitride chloride ZrNCl exhibits superconductivity below the superconducting critical temperature T_c of ~ 16 K by intercalation of alkali metal[1]. Experimental results have suggested that its superconducting properties are difficult to be explained by BCS theory[2]. Therefore, theoretical studies have proposed a model mediated by spin fluctuations[2] and a superconducting mechanism with a BCS-BEC crossover[3]. However, there are no experimental observations of the electronic structure by angle-resolved photoemission spectroscopy (ARPES) measurements, which makes it difficult to further explore the superconducting mechanism. This is due to the fact that alkali metal-inserted ZrNCl is easily oxidized in the atmosphere and that it is difficult to obtain large single-crystal samples. In this study, we prepared electron-doped ZrNCl by depositing alkali metals in vacuum on a relatively large parent material. The electronic structure of the prepared ZrNCl after alkali metal deposition was studied by ARPES.

Samples were prepared by vacuum evaporation on cleaved ZrNCl single crystals in ultrahigh vacuum using a Potassium(K) deposition source. ARPES measurements were performed at BL-9A in Hiroshima Synchrotron Radiation Center (HiSOR) using an R4000 electron analyzer (Scienta Omicron) with p-polarized light. The total energy resolution was set to approximately 50 meV for hν = 40 eV. All the measurements were performed at 13 K. The binding energies of samples were determined by referencing the Fermi energy (E_F) of gold electronically contacted with samples.

Figures 1(a) and 1(b) show the band dispersion along the Γ(A)-K(H) and Γ(A)-K(H)-M(L) lines of the bulk Brillouin zone(BZ) of ZrNCl after K deposition. In Fig. 1(a), we found dispersive bands having a local minimum or a local maximum at the M point of BZ, indicating that observation reflect band dispersions of the sample. The experimental dispersions have the top at the Γ(A) point and a bottom at the K(L) point, consistent with calculated band dispersions of non-doped β-ZrNCl [4]. Quantitatively, the valence band width estimated from the energy positions of the top (~ 2.95 eV) and bottom (~ 8.85 eV) of the valence band is 5.9 eV, slightly larger than the calculated value of 5.0 eV [4]. In Fig. 1(b), an electron-pocket like intensity distribution at the K point and near E_F is clearly observed. Doped electron carriers are expected to fill the bottom of conduction band at the K point. Since the observation is consistent with this simple expectation, the electron-pocket like structure is most provably the bottom of the conduction band which is filled with electron carrier by K deposition. The bottom of the conduction band at the K point is located at approximately 0.27 eV, indicating an indirect band gap of about 2.68 eV. This is larger than the calculated value of 1.8 eV [4]. On the other hand, the observed valence band width and the indirect band gap are in relatively good agreement with 6.1 eV and 2.5 eV calculated by Yin et al. using DFT HSE06 [5], respectively. The present study provides the first observation of the valence band structure of electron-doped ZrNCl.

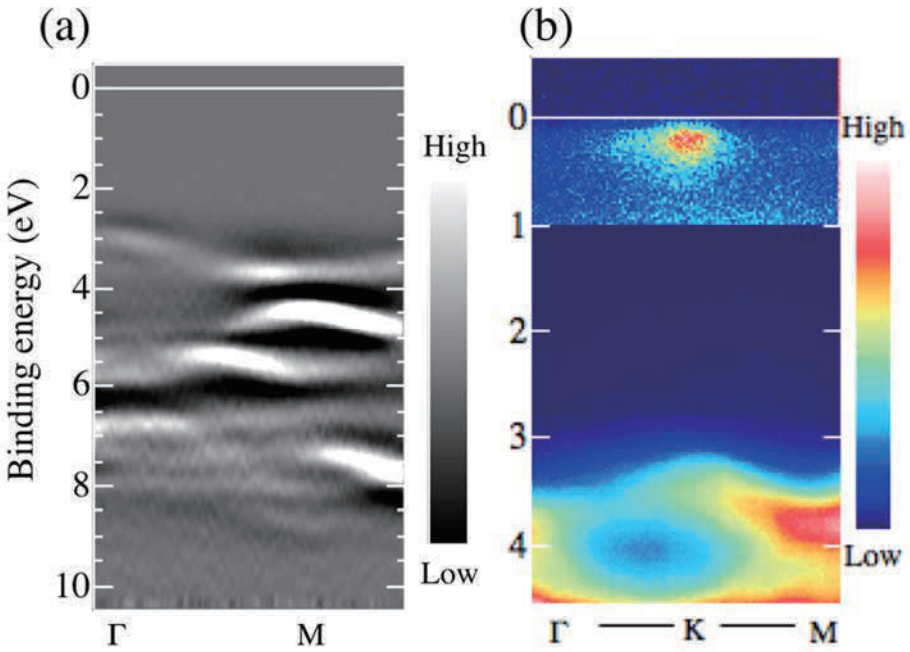

FIGURE 1. ARPES intensity maps of (a) the valence band along the Γ–M line and (b) near E_F along the Γ–K-M line. For (b), a narrower intensity window is set for the region near E_F, so that the weak structure can be observed easily.

REFERENCES

1. Y. Kasahara *et al.*, *Physica* C **514**, 354-367 (2015).
2. K. Kuroki, *Phys. Rev*. B **81**, 104502 (2010).
3. Y. Nakagawa *et al.*, *Science* **372**, 190 (2021).
4. H. Tanaka *et al.*, *J. Phys. Soc. Jpn.* **84**, 124706 (2015).
5. Z. P. Yin *et al.*, *Phys. Rev*. X **3**, 021011 (2013).

Study of Electronic State of Topological Heterojunction in Sb/Bi by Spin-resolved ARPES

H. Abe[a], M, Arita[b], K. Miyamoto[b], T. Okuda[b] and A. Takayama[a]

[a]*Department of Physics and Applied Physics, Waseda University, Okubo 3-4-1, Shinjuku, Tokyo 169-8555, Japan*
[b]*Hiroshima Synchrotron Radiation Center, Hiroshima University, Kagamiyama 2-313, Higashi-Hiroshima 739-0046, Japan*

Keywords: Topological surface state, Heterostructures, Spin-resolved ARPESA, Thin films.

Recently, in order to understand the intrinsic topological phase of materials and to explore potential materials for applications, a lot of studies focusing on topological phase transitions have been performed in various materials. The group-V semimetals bismuth (Bi) and antimony (Sb) are known to exhibit spin-splitting surface states at surfaces and interfaces, which called topological surface states and Rashba-type spin-splitting. Interestingly, it is predicted that Bi and Sb will undergo a topological phase transition due to lattice strain. For Bi, although it is classified as a topologically trivial material in bulk, it is theoretically predicted that slightly lattice-strain induces phase transition to topological semimetals (topologically nontrivial material) [1]. Indeed, it has been reported that less than 200 bilayer (BL) Bi thin films have topologically nontrivial band structure measured by angle-resolved photoemission spectroscopy (ARPES) [2]. For Sb, freestanding Sb(111) films with less than 4 BL have been reported to be topologically trivial [3] while Sb bulk crystal is classified as a topologically nontrivial material. Similarly with Bi, several calculations for Sb predicted that the topological phase transition can be induced by tuning structural parameters [4]. Topological phase transitions by epitaxial strain at the interface are very useful from the viewpoint of applications because they do not require any external field environment and are compatible with surface sensitive experimental technique. At the same time, clarifying the electronic structure of interfacial heterojunction with spin-polarized electronic states is important for the fundamental physics.

In this study, we performed spin-resolved ARPES for Sb/Bi hetero structure in order to clarify the spin state at the interface between Sb and Bi. The spin-resolved ARPES measurements were performed at BL9A/B, Hiroshima Synchrotron Radiation Center (HiSOR). Owing to the surface sensitivity of the photoelectron spectroscopy, we performed our experiments on a sample of ultrathin Sb film (2~3 BL) deposited on Bi thin film. Samples were prepared by room temperature deposition of Sb on Bi thin film on Si(111). To avoid the formation of the $Bi_{1-x}Sb_x$ alloy, no annealing process is applied. The 1 × 1 surface structure of the Sb/Bi heterostructure was confirmed by the low-energy electron diffraction (LEED) measurement.

Figure 1(a) shows the band structure for the 3BL-Sb thin film/Bi(111) near E_F around the $\bar{\Gamma}$ point . We observed the “V”-shaped electronic bands, which are significantly different from the electronic state of the Bi thin film and the freestanding Sb ultra-thin film. This is consistent with the results of our previous study [5]. To experimentally clarify the spin-polarized nature of the “V”-shaped band, we have performed a spin-resolved ARPES experiment. Figure 1(b) plots the spin-resolved energy distribution curves (EDCs) for the *y*-spin component measured at a representative angle θ along the k_x from the $\bar{\Gamma}$ point ($\theta = 0$). As seen in Fig. 1(b), the pin-resolved-EDCs of the “V”-shaped electronic bands in $+k_x$ region are dominated by the up spin, while the down spin is superior in $-k_x$ region. This indicates that the in-plane spin direction is basically reversed across the $\bar{\Gamma}$ point, qualitatively consistent with the Rashba picture. Free-standing 3BL Sb thin films theoretically have no spin-polarized component, suggesting that this spin-polarized component is due to the hybridization of the wavefunction of the Rashba splitting surface state of Bi with the one of Sb ultrathin films.

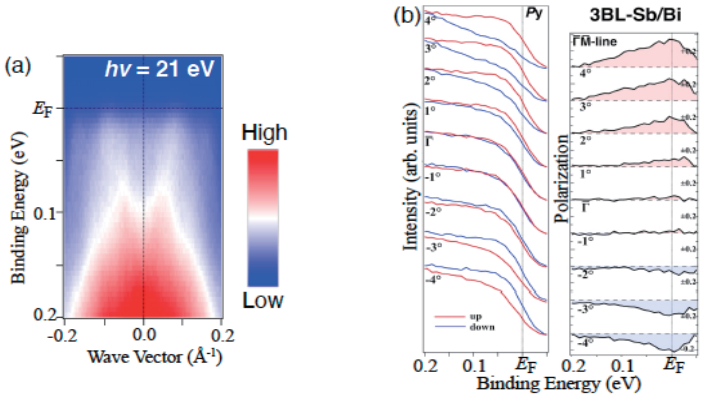

FIGURE 1. (a) the band structure for the 3BL-Sb thin film/Bi(111) near E_F around the $\bar{\Gamma}$ point . (b) spin-resolved EDC measured at a representative angle θ along the k_x.

REFERENCES

1. T. Hirahara, N. Fukui, T. Shirasawa, M. Yamada, M. Aitani, H. Miyazaki, M. Matsunami, S. Kimura, T. Takahashi, S. Hasegawa, and K. Kobayashi, Phys. Rev. Lett. **109**, 227401 (2012).
2. S. Ito, B. Feng, M. Arita, A. Takayama, R.-Y. Liu, T. Someya, W.-C. Chen, T. Iimori, H. Namatame, M. Taniguchi, C.-M. Cheng, S.-J. Tang, F. Komori, K. Kobayashi, T.-C. Chiang, and I. Matsuda, Phys. Rev. Lett. **117,** 236402 (2016).
3. P. Zhang, Z. Liu, W. Duan, F. Liu, and J. Wu, Phys. Rev. B **85**, 201410 (2012).
4. F.-C. Chuang, C.-H. Hsu, C.-Y. Chen, Z.-Q. Huang, V. Ozolins, H. Lin, and A. Bansil, Appl. Phys. Lett. **102**, 022424 (2013).
5. H. Abe, D. Iwasawa, M. Imamura, K. Takahashi, and A. Takayama, AIP Advances **13**, 055303 (2023).

Cross-section effects and dichroism in $MnBi_2Te_4$-Bi_2Te_3 heterostructures

Philipp Kagerer [a], Begmuhammet Geldiyev[a], Maximilian Ünzelmann[a], Masashi Arita[b], Kenya Shimada[b], Hendrik Bentmann[a,*], and Friedrich Reinert[a]

[a]*JMU Würzburg and Würzburg-Dresden Cluster of Excellence, Am Hubland, 97074 Würzburg, Germany*
[b]*Hiroshima Synchrotron Radiation Center, University of Hiroshima, Higashi-Hiroshima 739-0047, Japan*

[*]*Present address: Center for Quantum Spintronics (QuSpin), NTNU Trondheim, NO-7034 Trondheim, Norway*

Keywords: Topological Insulators, Electronic Structure, Magnetism, Photoemission, Epitaxy

With the discovery of Bi_2Te_3, as a prototypical 3D topological insulator (TI), ways of manipulating its topological properties including the search for novel topological phases have become a topic of high interest. On the path towards technological applications, especially undergoing a controlled phase transition to the quantum anomalous Hall (QAH) phase is seen as a promising route to achieve one-dimensional conducting edge channels with ballistic transport and spin selectivity. This can only be achieved by breaking time-reversal symmetry (TRS), protecting the 3D-TI state, e.g. by introducing magnetic order. Compared to previous attempts using magnetic interfaces or dilute magnetic doping, here we focus on introducing magnetism into the TI Bi_2Te_3 intrinsically by facilitating the closely related intrinsic antiferromagnetic TI $MnBi_2Te_4$ [1,2]. While the surface state of bulk $MnBi_2Te_4$ has already been studied extensively and the influence of the magnetism on the Dirac point has been found to be subtle [3-6], we have recently succeeded in imaging a clear magnetic gap opening in MBE grown $MnBi_2Te_4$-Bi_2Te_3 heterostructures [7].

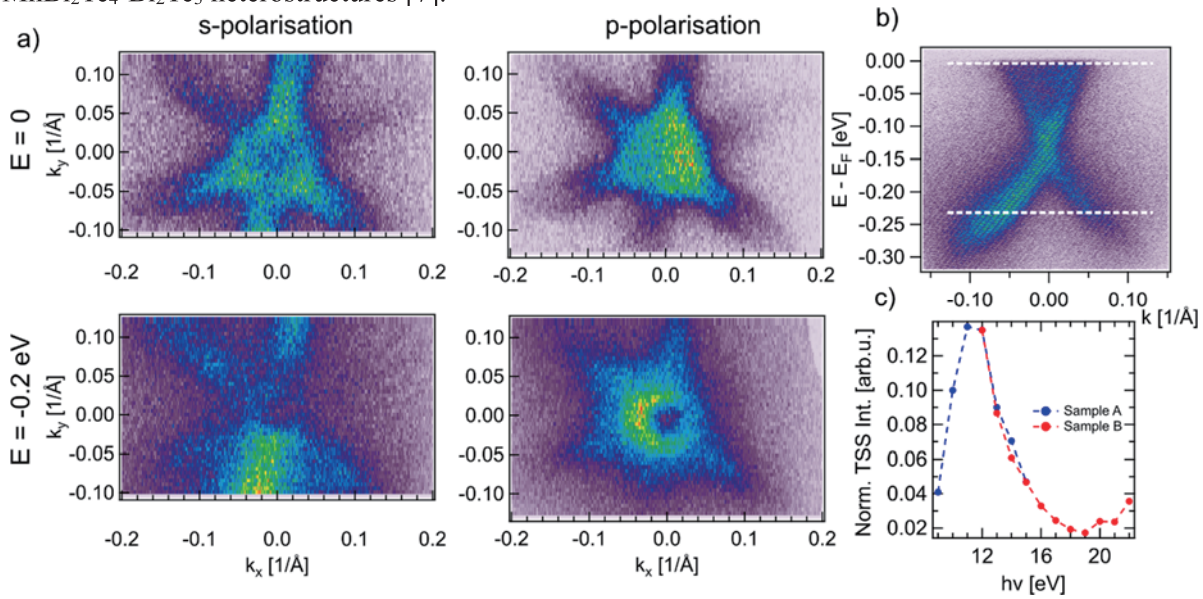

FIGURE 1. Dichroism and photon-energy dependent cross section of the $MnBi_2Te_4$ - Bi_2Te_3 heterostructure. a) Iso-energy surfaces of the Brillouin-zone center depicting the TSS of the heterostructure. The data was acquired at a photon energy of 12 eV and clearly depicts a switch in the dichroic behavior for incident p-polarized light, while showing a complex threefold symmetric pattern for s-polarization. b) Energy vs. k representation of the TSS at hv = 12 eV. The white lines indicate the positions of the iso-energy surfaces. c) Photon energy dependent cross section of the TSS, exhibiting a clear maximum at 12 eV.

Due to the peculiar z-profile of the heterostructure hosting a single SL of $MnBi_2Te_4$ at its surface, the photoemission cross-section of the TSS is highly non-trivial and may give insight into the real-space location of the respective DOS. Here we have studied the TSS especially in the low hv regime, for which beamline 9B is particularly suited. Our findings confirm a maximum of the cross-section at hv=12 eV and a monotonous decay towards both higher and lower energies. Measurements at this photon energy (hv=12 eV) with both linear light polarizations are depicted in Fig. 1a and allow us to obtain important insights on orbital symmetries of the TSS. Together with findings on the spin polarization conducted at BL-9B and the spin-LASER ARPES setup, the results let us profile the orbital and spin texture of the TSS and confirm its topological nature.

REFERENCES

1. M.M. Otrokov et al., Nature **576**, 416-422 (2019)
2. A. Zeugner et al., Chem. Mater. **31**, 8, 2795-2806 (2019)
3. R.C. Vidal et al., Phys, Rev. B **100**, 12104 (2019)
4. A.M. Shikin et al., Scientific Reports **10**, 13226 (2020)
5. Y.J. Hao et al., Phys. Rev. X **9**, 041038 (2019)
6. Y.J. Chen et al., Phys. Rev. X **9**, 041040 (2019)
7. P. Kagerer et al., Phys Rev. Res. **5**, L022019 (2023)

Electronic structure of thermoelectric semimetal $Ta_2Pd(Se_{1-x}S_x)_6$ studied by angle-resolved photoemission spectroscopy

D. Ootsuki[a], T. Ishida[a], M. Nagamoto [a], M. Arita[b], A. Nakano[c], U. Maruoka[c], I. Terasaki[c], and T. Yoshida[a]

[a] *Graduate School of Human & Environmental Studies, Kyoto University, Kyoto 606-8501, Japan,*
[b] *Hiroshima Synchrotron Radiation Center, Hiroshima University, Higashi-Hiroshima, 739-0046, Japan,*
[c] *Department of Physics, Nagoya university, Nagoya 464-8602, Japan.*

Keywords: Thermoelectric semimetal, angle-resolved photoemission spectroscopy, transition-metal chalcogenide

Thermoelectric effect has attracted much attention due to the potential for the energy harvesting. Recently, Nakano *et al.* have discovered that a transition-metal chalcogenide Ta_2PdSe_6 reveals a large Peltier conductivity $P = S\sigma$ [1,2]. The Seebeck coefficient S increases with decreasing temperature and shows the peak structure at $T = 20$ K. The coexistence of the enhancement of S and the high electrical conductivity σ derived from the semimetal causes the large Peltier conductivity [2]. Recent studies reported that the peak structure of S strongly depends on the anion substitution. In this study, we have performed the angle-resolved photoemission spectroscopy (ARPES) for $Ta_2Pd(Se_{1-x}S_x)_6$ (x = 0.00 and 0.05) at HiSOR BL-9A in order to clarify the origin of the enhancement of large Seebeck coefficient S.

Figures 1 (a) and (b) show the observed Fermi surfaces (FSs) for x = 0.00 and 0.05 taken at T = 20 K and $h\nu$ = 21 eV. The band dispersions around Γ point and X point are depicted in Figs. 1 (c) and (d). The hole pocket around Z point and the electron pockets at BZ boundary were identified. However, the topology of the FS for x = 0.05 is basically same as that for x = 0.00 and there is no significant difference in the band dispersions. Therefore, we speculate that the small differences of the quasiparticle electronic structure near E_F are responsible for the enhancement of S, which causes the large Peltier conductivity.

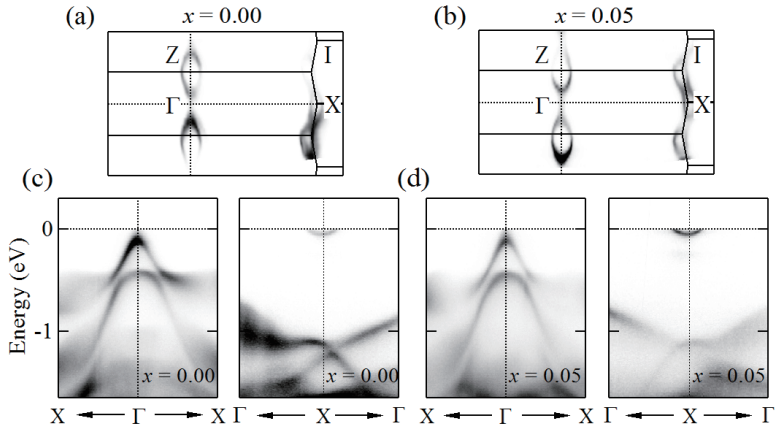

FIGURE 1. Fermi surfaces of $Ta_2Pd(Se_{1-x}S_x)_6$ of (a) x = 0.00 and (b) x = 0.05. Band dispersions around Γ point and X point of $Ta_2Pd(Se_{1-x}S_x)_6$ for (c) x = 0.00 and (d) x = 0.05., respectively. The data were collected at T = 20 K and $h\nu$ = 21 eV.

REFERENCES

1. A. Nakano, A. Yamakage, U. Maruoka, H. Taniguchi, Y. Yasui, and I. Terasaki, J. Phys. Energy **3**, 044004 (2021).
2. A. Nakano, U. Maruoka, F. Kato, H. Taniguchi, and I. Terasaki, J. Phy. Soc. Jpn. **90**, 033702 (2021).

Study on The Electronic Structure of Kagome Metal $Rh_3Pb_2S_2$

Zhanyang Hao[1], Yuan wang[1], Hongtao Rong[1], Yongqing Cai[1], Fayuan Zhang[1], and Chaoyu Chen[1]

Shenzhen Institute for Quantum Science and Engineering (SIQSE) and Department of Physics, Southern University of Science and Technology (SUSTech), Shenzhen 518055, China.

Keywords: Kagome metal, ARPES, band structure, topological state

The exploration of topological physics intertwined with non-trivial lattice geometries and strong electron interactions is emerging as a new frontier in condensed matter physics[1-6]. Kagome metals have attracted numerous attention due to the emergence of novel electronic state that can host van Hove singularity, Dirac cone and flat band. Various exotic phenomena can emerge from the interplay between nontrivial band topology and strong Coulomb correlations. Recently, a series of single crystals with Kagome lattice have been reported[3,7-22]. Exploring and preparing new single crystals with Kagome lattice can provide broad platforms for searching novel topological states and studying correlation effects. Herein, we synthesized a new Kagome metal $Rh_3Pb_2S_2$ which consists of Rh Kagome layer. By using angle-resolved photoemission spectroscopy (ARPES) of BL09A in HiSOR, the band structure of $Rh_3Pb_2S_2$ was preliminarily uncovered, which provided a reference for our follow-up research.

The crystal structure of $Rh_3Pb_2S_2$ (space group: *R*-3*m*, #166) is shown in Fig. 1 (a). Rh (red ball)-Pb (black ball) layer and Pb-S (yellow ball) layer stack along c-axis in which the Rh atoms form a Kagome lattice. The powder X-ray diffraction (XRD) pattern is plotted together with the simulated one, as shown in Fig.1 (b), which can demonstrate the quality and phase of the single crystals.

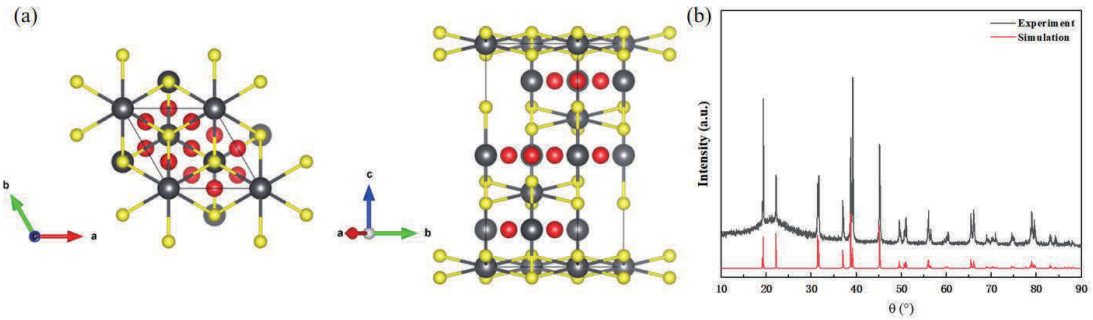

FIGURE 1. Crystal structure and XRD pattern of $Rh_3Pb_2S_2$. (a) Crystal structure of $Rh_3Pb_2S_2$. (b) Experimental and simulated powder XRD results.

To uncover the band structure of $Rh_3Pb_2S_2$, we perform ARPES measurement on the (00l)

cleaved plane. As shown in Fig. 2 (a), the hexagonal constant energy contour can be observed and can match well with the Brillouin zone plotted with the lattice parameter a = b =5.7 Å and c = 13.8 Å. To focus on the dispersion along K-M-K direction, as shown in Fig. 2 (b), a Dirac cone-like feature is observed, which may indicate its topological property and deserve further investigation.

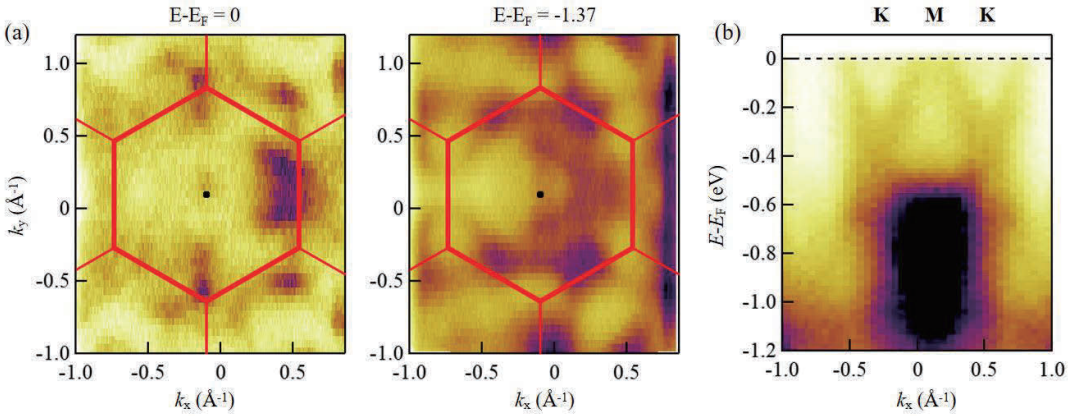

FIGURE 2. Band structure of $Rh_3Pb_2S_2$. (a) Constant energy contour at different binding energy E_B = 0 and E_B = 1.37 eV. (b) Electronic structure along K-M-K direction.

In a word, the ARPES results provide us with the detailed electronic structure of $Rh_3Pb_2S_2$, which provides a basis for our subsequent research.

REFERENCES

[1] S. Nakatsuji, N. Kiyohara, and T. Higo, Large anomalous Hall effect in a non-collinear antiferromagnet at room temperature, Nature **527**, 212 (2015).

[2] J.-X. Yin *et al.*, Giant and anisotropic many-body spin–orbit tunability in a strongly correlated kagome magnet, Nature **562**, 91 (2018).

[3] L. Ye *et al.*, Massive Dirac fermions in a ferromagnetic kagome metal, Nature **555**, 638 (2018).

[4] E. Liu *et al.*, Giant anomalous Hall effect in a ferromagnetic kagome-lattice semimetal, Nat. Phys. **14**, 1125 (2018).

[5] J.-X. Yin *et al.*, Negative flat band magnetism in a spin–orbit-coupled correlated kagome magnet, Nat. Phys. **15**, 443 (2019).

[6] D. Liu *et al.*, Magnetic Weyl semimetal phase in a Kagomé crystal, Science **365**, 1282 (2019).

[7] B. R. Ortiz *et al.*, New kagome prototype materials: discovery of KV3Sb5, RbV3Sb5, and CsV3Sb5, Phys. Rev. Mater. **3** (2019).

[8] B. R. Ortiz *et al.*, Cs V 3 Sb 5: A Z 2 Topological Kagome Metal with a Superconducting Ground State, Phys. Rev. Lett. **125**, 247002 (2020).

[9] B. C. Sales, J. Yan, W. R. Meier, A. D. Christianson, S. Okamoto, and M. A. McGuire, Electronic, magnetic, and thermodynamic properties of the kagome layer compound FeSn, Phys. Rev. Mater. **3**, 114203 (2019).

[10] T. Kida, L. Fenner, A. Dee, I. Terasaki, M. Hagiwara, and A. Wills, The giant anomalous Hall effect in the ferromagnet Fe3Sn2—a frustrated kagome metal, J. Phys.: Condens. Matter **23**, 112205 (2011).

[11] L. Ye *et al.*, de Haas-van Alphen effect of correlated Dirac states in kagome metal Fe3Sn2, Nat. Commun. **10**, 4870 (2019).

[12] T. Asaba, S. M. Thomas, M. Curtis, J. D. Thompson, E. D. Bauer, and F. Ronning, Anomalous Hall effect in

the kagome ferrimagnet
GdMn6Sn6, Phys. Rev. B **101** (2020).
[13] J. X. Yin *et al.*, Quantum-limit Chern topological magnetism in TbMn6Sn6, Nature **583**, 533 (2020).
[14] Q. Wang *et al.*, Large intrinsic anomalous Hall effect in half-metallic ferromagnet Co3Sn2S2 with magnetic Weyl fermions, Nat. Commun. **9**, 1 (2018).
[15] S. N. Guin *et al.*, Zero-Field Nernst Effect in a Ferromagnetic Kagome-Lattice Weyl-Semimetal Co3Sn2S2, Adv. Mater. **31**, 1806622 (2019).
[16] N. Morali *et al.*, Fermi-arc diversity on surface terminations of the magnetic Weyl semimetal Co3Sn2S2, Science **365**, 1286 (2019).
[17] S. Peng *et al.*, Realizing Kagome Band Structure in Two-Dimensional Kagome Surface States of RV_6Sn_6 (R=Gd, Ho), Phys Rev Lett **127**, 266401 (2021).
[18] H. Ishikawa, T. Yajima, M. Kawamura, H. Mitamura, and K. Kindo, GdV6Sn6: A Multi-carrier Metal with Non-magnetic 3d-electron Kagome Bands and 4f-electron Magnetism, J. Phys. Soc. Jpn. **90**, 124704 (2021).
[19] G. Pokharel, S. M. Teicher, B. R. Ortiz, P. M. Sarte, G. Wu, S. Peng, J. He, R. Seshadri, and S. D. Wilson, Electronic properties of the topological kagome metals YV 6 Sn 6 and GdV 6 Sn 6, Physical Review B **104**, 235139 (2021).
[20] X. Teng *et al.*, Discovery of charge density wave in a kagome lattice antiferromagnet, Nature **609**, 490 (2022).
[21] J. X. Yin *et al.*, Discovery of Charge Order and Corresponding Edge State in Kagome Magnet FeGe, Phys Rev Lett **129**, 166401 (2022).
[22] Y. Wang *et al.*, Flat Band and $\mathbb{Z}2$ Topology of Kagome Metal CsTi3Bi5, Chin. Phys. Lett. **40**, 037102 (2023).

Evolution of Electronic States in Epitaxial YBCO Thin Films with Calcium Doping by Angle-Resolved Photoemission Spectroscopy

Anjana Krishnadas[a], Yuita. Fujisawa[a], Markel Pardo-Almanza[a], Kohei Yamagami[a,b], Yukiko Obata[a], Yoshinori. Okada[a]

[a]*Quantum Materials Science Unit, Okinawa Institute of Science and Technology (OIST), Okinawa 904-0495, Japan.*

[b]*Japan Synchrotron Radiation Research Institute, Hyogo, 679–5198, Japan.*

Keywords: High temperature superconductors, ARPES, epitaxial thin film growth, heterostructures.

Abstract

Cuprates are among the most intriguing strongly correlated systems, exhibiting a variety of complex electronic phases. Studies on the nature of the Fermi surface (FS) and the electronic properties of HTSCs such as $YBa_2Cu_3O_{7-d}$ (YBCO) have also gained attention thanks to powerful experimental technologies [1,2] and advances in thin film growth [3,4]. The development of film-based heterostructures is a new major challenge.

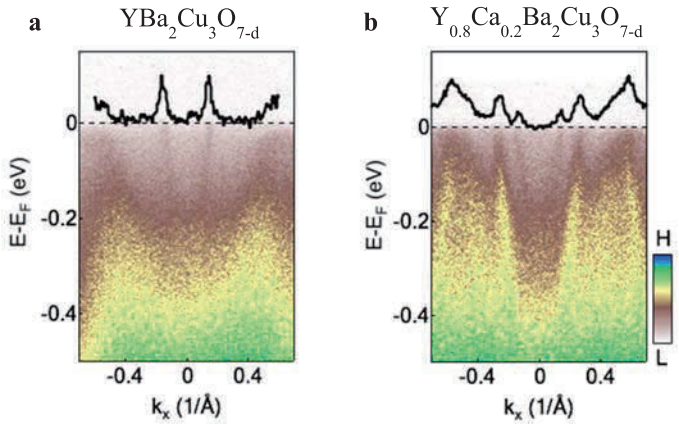

Figure 1. (a) ARPES intensity image of a near-optimally doped YBCO and (b) 20% Ca-doped thin film at the antinodal region obtained at 15 K, with a laboratory-based He-II light source (40.8 eV). The film was grown on a $LaAlO_3$(001) substrate.

In this work, we present an *in-situ* ARPES study on the calcium doping evolution of electronic states on the surface of YBCO epitaxial films grown by pulsed laser deposition. The ARPES of undoped YBCO shows the typical electronic structure of an optimally doped CuO_2 plane and a series of one-dimensional bands originating from the CuO chains, while the 20% Ca-doped YBCO thin film additionally shows a second chain state as shown in Figure (1 b). When YBCO is partially doped with Ca, we also observe

the appearance of band folding due to possible surface reconstructions. The careful tuning of the surface electronic states, together with a high Tc, as well as a larger coherence length along the c-axis, thus makes YBCO a good candidate as an HTSC substrate for *in-situ* heterostructures.

References:

[1]. H. Iwasawa *et al.*, *Phys. Rev. B.* 99 (14), 140510 (2019).
[2]. H. Iwasawa *et al.*, Ultramicroscopy, Volume 182, Pages 85-91 (2017).
[3]. Wu, Z.-B. *et al*., *Phys. Rev. Mater.* 4, 124801 (2020).
[4]. Y. Sassa et.al*., Phys. Rev. B* 83, 140511(R) (2011).

Observation of Spin-resolved Band Structure in Fe_3Ga Thin-films

K. Ohwada[a], K. Nakanishi[a], K. Kuroda[a,b], K. Miyamoto[c], T. Okuda[c], W. Zhou[d], S. Isogami[d], K. Masuda[d], Y. Sakuraba[d,e] and A. Kimura[a,b]

[a]*Graduate School of Advanced Science and Engineering, Hiroshima University, Higashi-Hiroshima 739-8526, Japan*
[b]*International Institute for Sustainability with Knotted Chiral Meta Matter (WPI-SKCM^2), Higashi-Hiroshima 739-8526, Japan*
[c]*Hiroshima Synchrotron Radiation Center, Hiroshima University, Higashi-Hiroshima 739-0046, Japan*
[d]*National Institute for Materials Science, Tsukuba 305-0047, Japan*
[e]*PRESTO, Japan Science and Technology Agency, Saitama 332-0012, Japan*

Keywords: Anomalous Nernst conductivity, Berry curvature, Spin-ARPES, Transverse Thermoelectric Conversion

Thermoelectric conversion from waste heat into electricity has shown great promise as sustainable energy sources. Up to now, thermoelectric conversion technology has developed mainly based on the Seebeck effect, in which carriers move along a thermal gradient and generate a voltage in a direction parallel to the heat flow. For practical application, it requires a three-dimensional geometry, resulting in the increase in manufacturing costs associated with larger and more highly integrated devices. In addition, the materials known so far to exhibit remarkable thermoelectric performance based on the Seebeck effect have disadvantages such as containing hazardous elements and noble metals and being mechanically fragile, which may explain why thermoelectric conversion is not yet widely used despite active research over the past few decades. Another approach to thermoelectric conversion is known as the Nernst effect, in which an electric voltage is generated in a direction orthogonal to the magnetic field and heat flow. However, this conventional ordinary Nernst thermopower requires an external magnetic field which hinders a usage in practical applications. Ferro- or ferrimagnetic materials with spontaneous magnetization exhibit the Nernst effect under no magnetic field. This is called the anomalous Nernst effect (ANE). The orthogonality of electric voltage and heat flow as well as the absence of an external magnetic field allows us to make curved devices that can be miniaturized and to reduce the manufacturing cost simultaneously. In 2017, an ANE with a thermopower of ~3 μV/K was found in $Fe_{0.85}Ga_{0.15}$ galfenol [1]. The significance of this finding is that the observed thermopower was two orders of magnitude higher than that of pure Fe (-0.1 μV/K) [2]. Nakayama *et al*. systematically investigated ANEs in disordered $Fe_{1-x}Ga_x$ thin films with different Ga atomic compositions and found that the magnitude of ANEs increased with increasing x, reaching a maximum thermopower (2.4 μV/K) at x = 0.32 [3]. Recently, an enhancement of ANE to 4 μV/K was reported for the ordered ($D0_3$) phase of Fe_3Ga bulk crystals, suggesting that a well-defined band structure is the key to the enlarged ANE [4].

The origin of the large ANE in the previous study [4] was essentially discussed through a comparison between experimental ANE and theoretical band structures. The transverse anomalous Nernst conductivity (a_{xy}) obtained from the calculated Berry curvature is generally very sensitive to energy, even changing its sign with energy shifts of 100-200 meV. Given that the Fermi energy positions depend on the choice of computational method and muffin-tin potential, the a_{xy} may be incorrectly displayed. The previous transport study also pointed out the importance of the Fermi energy position by the indirect comparison with the calculation [4]. In order to scrutinize the origin of ANEs and improve it, it is crucial to monitor experimentally the three-dimensional band structure and the location of the Fermi level of the “real” materials. Angle resolved photoelectron spectroscopy (ARPES) is a powerful tool for visualizing the band structure in materials. Combined with synchrotron radiation, it is, in principle, possible to reveal band structure along both in-plane and out-of-plane electron momentum. However, it has been applied only to a limited range of samples that can be easily cleaved in an ultra-high vacuum (UHV) condition mainly due to

surface sensitivity. In this sense, Fe-Ga bulk crystals are not suitable for this purpose due to the difficulty in cleaving samples. To the best of our knowledge, no experimental results with ARPES of Fe-Ga alloys have been reported so far. Furthermore, it is essential to elucidate the spin characteristics of the band structure. However, the lack of remanent magnetization in bulk samples has made it impractical to perform spin-resolved ARPES.

Here we investigate the spin-resolved band structure of ordered Fe_3Ga thin films and provide insight into the mechanism of their substantial ANE. We grew thin films of Fe_3Ga on MgO(001) substrate by UHV magnetron-sputtering method. The thin films were then transported to the spin-ARPES apparatus utilizing an UHV suitcase. In fact, well-ordered and clean surfaces were obtained by post-annealing in UHV.

The thin film samples were deposited on MgO(001) substrate *via* magnetron sputtering method at NIMS (Tsukuba) and transferred to the spin-ARPES apparatus (Hiroshima Univ.) using the vacuum suitcase. Spin-ARPES measurements were conducted at the ESPRESSO end-station (BL-9B) in the Hiroshima Synchrotron Radiation Center (HiSOR) [5]. The samples were annealed at 490 °C for 30 min at the preparation chamber prior to the spin-ARPES measurement. A magnetic field as large as ~0.5 T was applied to the samples along the [110] in-plane easy-axis using a permanent magnet in the preparation chamber at room temperature, which realizes almost total remanent magnetization to the [110] direction because of large shape magnetic anisotropy energy to the normal direction to the film surface.

The ARPES image of $Fe_{72}Ga_{28}$ (Ga rich) thin film was acquired in [110] direction acquired with a photon energy of 60 eV. We find steeply dispersive bands that cross the Fermi level (E_F) around $k_{||} = \pm 0.5$ Å^{-1}. No recognizable features are observed for $|k_{||}| < 0.5$ Å^{-1} above E-E_F = -1.0 eV, whereas less dispersive features with the rather strong intensity are observed at E-E_F = -1.0 ~ -1.5 eV. The spin-resolved energy distribution curves (EDC) at $k_{||} = 0$ Å^{-1} (cut 1), 0.60 Å^{-1} (cut 2), 0.79 Å^{-1} (cut 3) and 1.12 Å^{-1} (cut 4) were taken. Minority-spin EDCs show a peak near E-E_F = 0 eV, which confirms a minority spin character for the steeply dispersive bands crossing E_F near $k_{||} = \pm 0.5$ Å^{-1}.The minority-spin EDC at $k_{||} = 0$ Å^{-1} (cut 1) shows a single peak at E-E_F = -1.1 eV, while the majority-spin counterpart exhibits a broad feature at the similar energy that can be roughly decomposed into two intensity maxima at -1.0 and -1.2 eV. It tells us that the less dispersive feature near $k_{||} = 0$ Å^{-1} involves three distinctive bands possessing majority, minority and majority spin characteristics at E-E_F = -1.0, -1.1 and -1.2 eV, respectively. All of the experimental results shown here are reasonably explained by the calculated band structures using the first principles calculation when the theoretical E_F is shifted downward (toward higher binding energy) by about 100 meV.

We have also performed the same experiment for the stoichiometric Fe_3Ga film and obtained almost the same result except for the position of the Fermi level. It is found that the difference of the Fermi level between calculation and experiment is reduced to 30 meV with little modification of band features. In fact, this film achieves the Nernst voltage of 4.0 μVK^{-1}, which is comparable to the bulk value [4]. The calculated transverse thermoelectric conductivity α_{xy} reproduces the experimental value. We then conclude that the observed high anomalous Nernst effect originates from the Berry curvature generated from the internal band structure.

The experiment was carried out at BL9B of HiSOR (Proposal Nos. 19BG050, 20AG057). This work was financially supported by JSPS KAKENHI (Grants No. 17H06152, No. 18H03683).

REFERENCES

1. Z. Yang, E. A. Codecido, J. Marquez, Y. Zheng, J. P. Heremans, and R. C. Myers, AIP Adv. **7**, 095017 (2017).
2. S. J. Watzman, R. A. Duine, Y. Tserkovnyak, S. R. Boona, H. Jin, A. Prakash, Y. Zheng, and J. P. Heremans, Phys. Rev. B **94**, 144407 (2016).
3. H. Nakayama, K. Masuda, J. Wang, A. Miura, K. Uchida, M. Murata, and Y. Sakuraba, Phys. Rev. Mater. **3**, 114412 (2019).
4. A. Sakai, S. Minami, T. Koretsune, T. Chen, T. Higo, Y. Wang, T. Nomoto, M. Hirayama, S. Miwa, D. Nishio-Hamane, F. Ishii, R. Arita, and S. Nakatsuji, Nature **581**, 53 (2020).

Spin Polarization of the electronic states of Pb adsorbed Si(001) Surface

Sakura N. Takeda[a], Yuya Kaida[a], Takaaki Tamura[a], Taiga Itoh[a], Koji Miyamoto[b], Taichi Okuda[b], Kazuyuki Sakamoto[c]

[a]*Nara Institute of Science and Technology, 8916-5, Takayama-cho, Ikoma-shi, Nara, Japan 630-0101*
[b]*Hiroshima University, 1-3-2 Kagamiyama, Higashi-Hiroshima City, Hiroshima, Japan 739-8511*
[c]*Osaka University, 2-1 Yamadaoka, Suita, Osaka 565-0871*
Keywords: Si(001), Pb, surface states, semiconductor, valence bands.

Stimulated by the discoveries of the unique phenomena in Pb ultrathin (one or two monolayer-thick) films on Si(111) and Ge(111) surfaces, such as superconducting (SC) transition [1], Rashba spin splitting [2], and strong electron accommodation ability [3], Pb adsorbed Si(001) surfaces have recently attracted much attention [4,5]. Matetskiy [5] and Bondarenko [6] reported a SC transition at the Si(001)c(4×4)-Pb surface at Tc=1.3 K, which is well below the Tc of bulk Pb (7.2 K) but close to that for Si(111)$\sqrt{3}\times\sqrt{3}$-SIC-Pb (1.83K). At the Si(001) 2×1-Pb surface, on the other hand, no SC transition has been observed so far. The Pb coverage of the Si(001) 2×1-Pb and c(4×4)-Pb surfaces are reported to be 1.5ML and 1.875 ML, respectively [4]. Even though the two surfaces have similar Pb coverage, one surface exhibits the SC transition, and the other does not. This discrepancy should be explained in terms of the electronic structure, including spin. Thus, in this work, we studied the spin-polarized electronic structure of Si(001) 2×1-Pb using ARPES and SARPES at beamline BL-9B of HiSOR.

The sample preparation was done in the preparation chamber of BL-9B. A p-type Si(001) wafer (B-doped, 5-10 ohm cm) was used as the substrate. After degassing, the sample was flash-annealed to obtain a clean Si(001)2×1 surface. Subsequently, Pb was deposited onto the surface to make Si(001) (2×1)-Pb. The surface structure was monitored using RHEED throughout the sample preparation. The in-plane (Sx, Sy) and out-of-plane (Sz) spin components of the electron were obtained by using the very low energy electron diffraction (VLEED) spin polarimeters of the SARPES apparatus (Efficient Spin-resolved Spectroscopy Observation machine: ESPRESSO).

Figure 1 (a) shows the crystal orientations of the sample. Figure 1(b) shows the ARPES intensity map of Si(001) (2×1)-Pb along the [110] direction. The photon energy was 21 eV. The top of the Si valence band and the (2×1)-Pb surface states are observed in Fig. 1(b). SARPES spectra were measured at several emission angles along the [110] direction. The spin-resolved EDCs along the y ($[\bar{1}10]$) direction are shown in Figs. 1(c). While the EDCs of up- and down-spin at 0° are degenerate, the position of some peaks in the up- and down-spin EDCs differs at non-zero emission angles. Spin components in the other directions (x and z) were found to be degenerate. This result supports that the surface states of the Si(001) (2×1)-Pb are spin-polarized

under the Rashba-type spin-splitting mechanism.

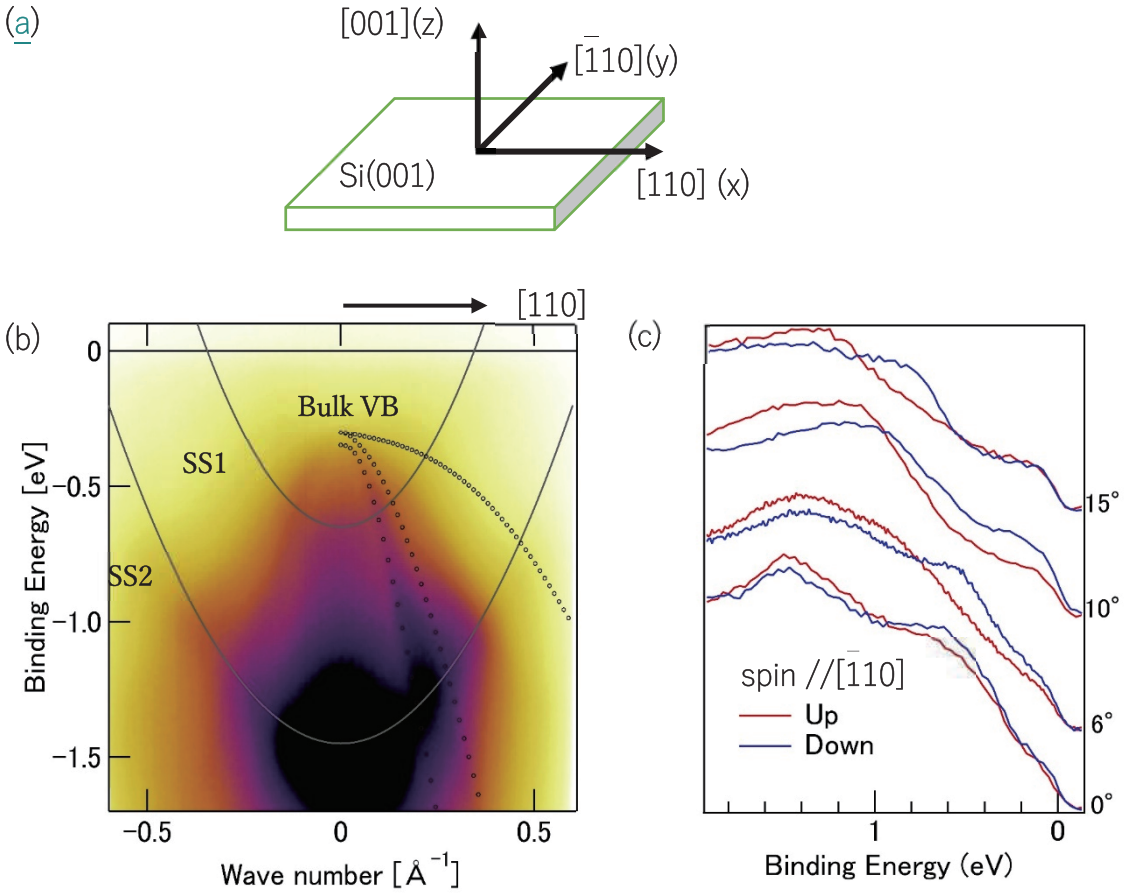

FIGURE 1. (a) In-plane and out-of-plane crystal orientations of the sample. (b) ARPES intensity map of Si(001) 2x1-Pb surface along [110]. The dotted lines are Si bulk valence bands, and the solid lines are guide to the eye to show the surfaces states. (c) EDCs for up- and down-spin states obtained by SARPES along [110]. The spin polarization is along [$\bar{1}$10].

REFERENCES

[1] T. Zhang *et al.*, Nat. Phys. **6**, 104 (2010).
[2] K. Yaji *et al.*, Nat. Commun. **1**, 1 (2010).
[3] S. N. Takeda, N. Higashi, and H. Daimon, Phys. Rev. B **82**, 35318 (2010).
[4] V. G. Kotlyar *et al.*, Surf. Sci. **695**, 121574 (2020).
[5] A. V. Matetskiy *et al.*, Surf. Sci. **708**, 121822 (2021).
[6] L. V. Bondarenko *et al.*, J. Phys. Chem. Lett. **13**, 10479 (2022).

Spin Texture of Te-Based Monolayer Materials

Begmuhammet Geldiyev[a], Maximilian Ünzelmann[a], Philipp Kagerer[a], Koji Miyamoto[b], Taichi Okuda[b], Takuma Iwata[c,d], Kenta Kuroda[c,d], Kenya Shimada[b], Hendrik Bentmann[a,*], and Friedrich Reinert[a]

[a]*JMU Würzburg and Würzburg-Dresden Cluster of Excellence, Am Hubland, 97074 Würzburg, Germany*
[b]*Hiroshima Synchrotron Radiation Center, University of Hiroshima, Higashi-Hiroshima 739-0047, Japan*
[c]*Graduate School of Advanced Science and Engineering, Hiroshima University, 1-3-1 Kagamiyama, Higashi-Hiroshima, Japan*
[d]*International Institute for Sustainability with Knotted Chiral Meta Matter (WPI-SKCM^2), Hiroshima University, Higashi-hiroshima 739-8526, Japan*

[*]*Present address: Center for Quantum Spintronics (QuSpin), NTNU Trondheim, NO-7034 Trondheim, Norway*

Keywords: Spin-resolved ARPES, 2D monolayer materials, Rashba effect, magnetic topological insulators

The combination of spin-orbit coupling (SOC) and inversion symmetry breaking (ISB) in crystalline solids fundamentally allows for a lifting of spin-degeneracy and a formation of spin-polarized electronic states. This effect underlies the physics of many two-dimensional (2D) quantum systems such as the surface states of topological insulators (TI) and Weyl semimetals, as well as Rashba-systems (RS) and thin-film materials, whose thickness goes down to few atomic layers. Moreover, recently, a novel class of topological quantum matter has been discovered; the so-called intrinsic magnetic TI [1]. This class of materials describes systems, in which magnetism and a topologically nontrivial electronic structure are combined intrinsically in the crystalline structure of a material without additional disorder by e.g. doping. The first discovered material of this kind is the van der Waals crystal $MnBi_2Te_4$ (MBT), in which the magnetism is introduced by a Mn sub-layer, with a strong intra- and a weak inter-layer coupling. This results in a quasi-two-dimensional A-type antiferromagnetic order, additionally stabilized by a strong out-of-plane anisotropy, which is stable even down to the monolayer limit.
Here we investigated the spin texture of three different families of Te-based monolayer systems using spin-resolved ARPES:

(i) honeycomb monolayers AgTe and CuTe, grown on Ag(111) and Cu(111), respectively
(ii) a Te square lattice on Au(100)
(iii) a monolayer $MnBi_2Te_4$ grown on epitaxial Bi_2Te_3 – films.

To this end, spin-APRES experiments were carried out at the “ESPRESSO” endstation at BL-9B as well as at the Laser-ARPES setup in the case of monolayer MBT (iii).
First, we studied the epitaxial binary honeycomb systems AgTe and CuTe (i). Other than a rigid energy shift, the band structure of these systems is similar and exemplarily shown for AgTe in Fig.1(a). In particular, one finds two occupied Te-derived surface states α and β, with a Rashba-type spin-orbit splitting observed for the lower-lying state β. While the band dispersion is well established already [2,3], we have experimentally verified the spin texture here for the first time, i.e., we particularly observe a helical in-plane spin texture (see Fig.1(a), right panels) [4]. It should be noted that, in contrast to AgTe, no Rashba splitting can be experimentally detected in the spin-integrated ARPES measurements on CuTe [3], indicating a presumably smaller Rashba parameter in this case. Based on our spin-resolved measurements, we were now able to observe a spin-orbit splitting in the β-band of CuTe as well (see Fig.1(a), right panels) [4].
Next, we investigated a Te square lattice on a Au(100) substrate (ii) [5]. Here, we focused on the anisotropic Rashba splitting around the two-fold symmetric X point in the Brillouin zone of the square lattice (see Fig. 1(b)). Spin-ARPES measurements provide direct experimental evidence for a Rashba-type spin polarization

around X, as predicted from density functional theory calculations.
Lastly, the spin texture in the topological surface state of a monolayer MBT on Bi_2Te_3 was studied. Using synchrotron- as well as Laser-based spin-ARPES experiments, we could verify the characteristic spin-momentum locking in the Dirac cone, as shown in Fig. 1(c).
In summary, we have investigated the in-plane helical spin textures in distinct Te-based 2D quantum materials. Our experimental results clearly confirm a Rashba-type spin-momentum locking in the respective surface states. The data are part of two manuscripts, which are currently under review [5] or in preparation [4].

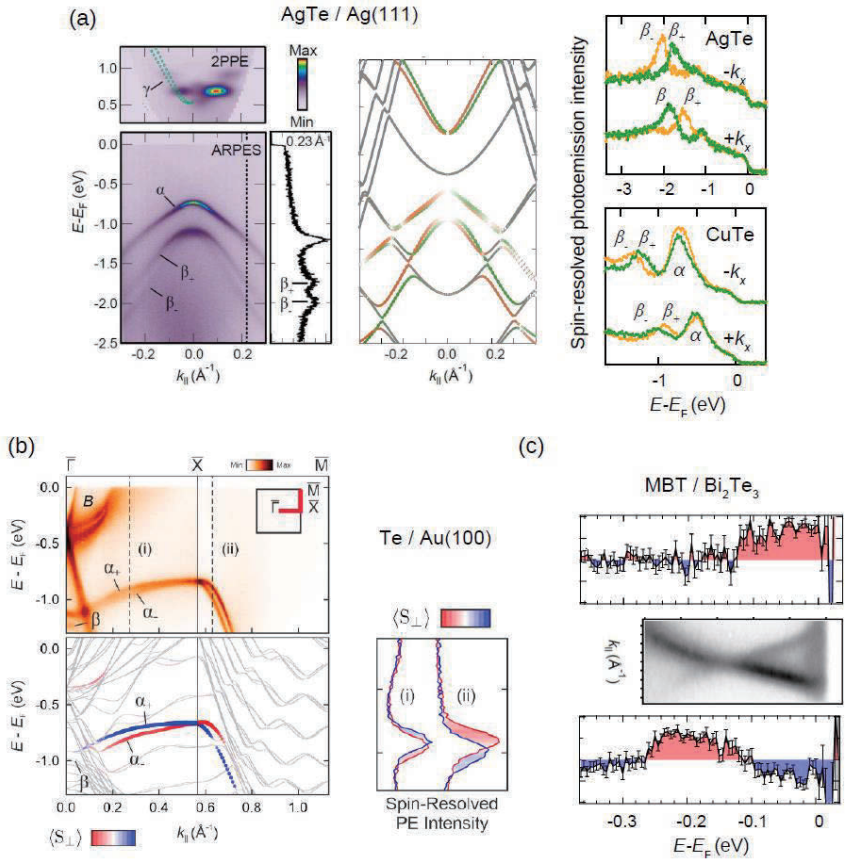

FIGURE 1. (a) Band structure and Rashba-type spin polarization of binary honeycomb monolayers AgTe and CuTe. The left and middle panel is taken from [6]. Spin-resolved photoemission data in the right panels were conducted at BL-9B and show the Rashba spin component S_y along $\pm k_x$ [4]. (b) Band structure and spin-resolved ARPES on the Te/Au(100) system (taken from [5]). (c) Spin-integrated ARPES spectrum of the TSS of a MBT-BT heterostructure. Upper and lower panels correspond to the measured spin polarization along energy distribution curves at ±0.03 $Å^{-1}$ and depict a high degree of spin polarisation in the TSS. (taken from [7]).

REFERENCES

1. M.M. Otrokov et al., *Nature* **576**, 416-422 (2019).
2. M. Ünzelmann et al., *Physical Review Letters* **124**, 176401 (2020).
3. Y. Tong et al., *2D Materials* **7**, 035010 (2020).
4. B. Geldiyev, M. Ünzelmann et al., (in preparation).
5. B. Geldiyev et al., arXiv:2308.02372 (2023).
6. M. Ünzelmann, "Interplay of Inversion Symmetry Breaking and Spin-Orbit Coupling – From the Rashba Effect to Weyl Semimetals" Ph.D. Thesis, University of Würzburg 2022.
7. P. Kagerer, "Two-dimensional Ferromagnetism and Topology at the Surface of $MnBi_2Te_4$-Bi_2Te_3 Heterostructures – MBE-growth, Magnetism and Electronic Properties" Ph.D. Thesis, University of Würzburg 2023.

Spin texture of V-intercalated transition metal dichalcogenide $V_{1/3}NbS_2$

Fayuan Zhang[1], Hongtao Rong[1], Yuan Wang[1], Zhanyang Hao[1], Yongqing Cai[1], and Chaoyu Chen[1]

[1] *Shenzhen Institute for Quantum Science and Engineering (SIQSE) and Department of Physics, Southern University of Science and Technology (SUSTech), Shenzhen 518055, China.*

Keywords: spin-valley locking, altermagnetism, spin-resolved ARPES

Spin–valley locking is ubiquitous among transition metal dichalcogenides, in turn stabilizing properties such as Ising superconductivity, and opening routes towards ‘valleytronics’. The related spin-valley splitting is caused by spin–orbit coupling and can be tuned via the application of external magnetic fields or through proximity coupling with ferromagnetic layers. V-intercalated transition metal dichalcogenide V1/3NbS2 is an interesting candidate, NbS2 layers are next to ferromagnetic V layers[1, 2], therefore, V1/3NbS2 is natural an ideal platform to study the effect of magnetic proximity. On the other hand, V1/3NbS2 is regarded as a candidate of altermagnet[3-5]. Spin-resolved ARPES is a powerful tool to reveal these properties. However, study based on spin-resolved ARPES have not been conducted to date. Here, we investigate the spin texture of band structure of the V-intercalated transition metal dichalcogenide V1/3NbS2 using spin-resolved ARPES build at HiSOR.

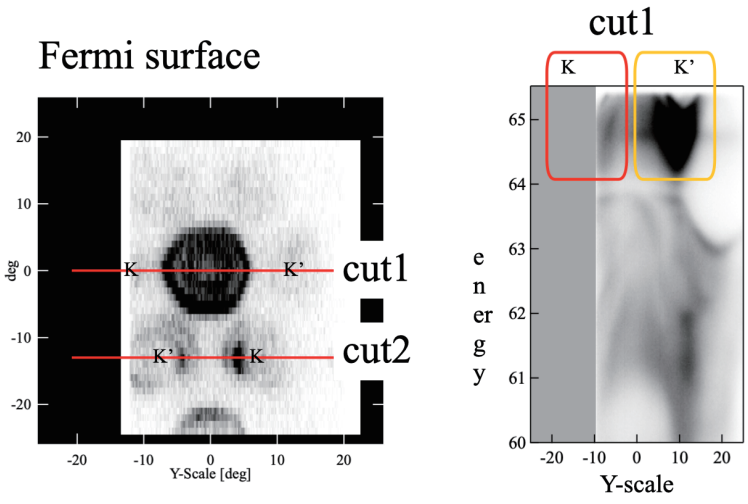

Fig. 1 Fermi surface of $V_{1/3}NbS_2$ and spin integrated cut along K’ΓK (cut1).

The sample was cleaved at 40 K, and tuned the angles of the sample to obtain the targeted direction Γ-K along the slit of analyzer by quick maps, the final Fermi surface is shown in Fig. 1. Our experiment focus on the cut1 and cut2 shown in the left figure of Fig. 1. The red and yellow frames are used to indicate K and K' points, respectively. Spin-resolved data corresponding to K and K' of cut1 are shown in Fig. 2 and Fig. 3.

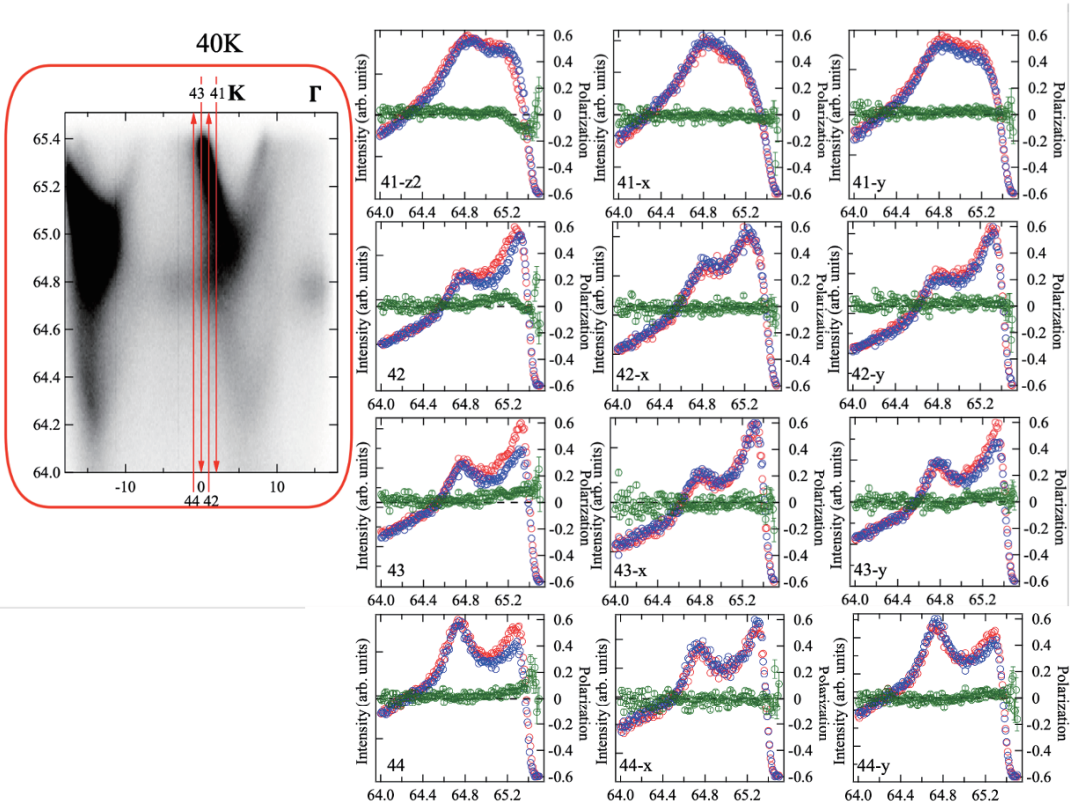

Fig. 2 Spin resolved data of the vally near K of cut1

Combined with the data shown in Fig. 2 and Fig. 3, we can tell the opposite splitting at K' and K. Spin-resolved data near K' of cut2 are shown in Fig. 4 and Fig. 5, similarly, the spin polarization on the two sides of K' is opposite. To distinguish the spin-valley and altermagnetic splitting, we conducted the temperature dependent test focus on line 28 in Fig. 4, the result show that no obvious change has been observed.

In summary, the spin splitting observed here comes from the spin-orbit coupling instead of altermagnetism. As for the altermagnetic splitting, maybe we should conduct

the experiment in other direction, such as ΓM, and this is the part of our next experiment plan.

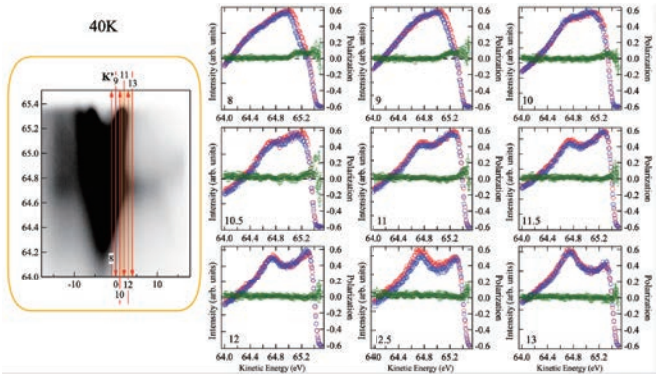

Fig. 3 Spin resolved data of the vally near K' of cut1

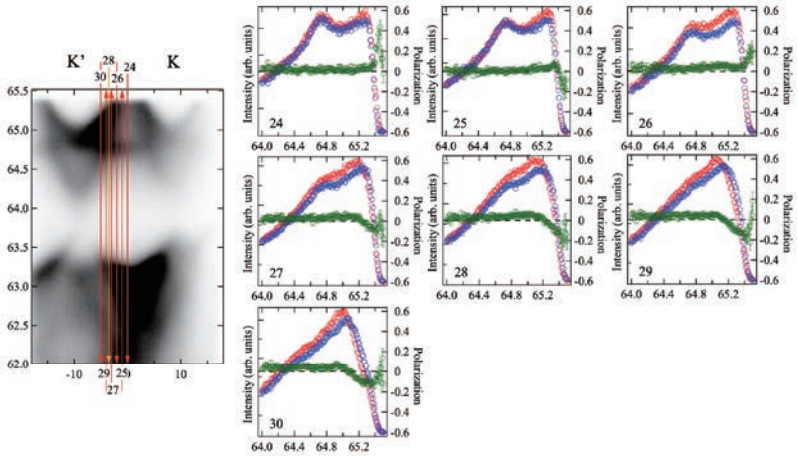

Fig. 4 Spin resolved data of the vally near K' of cut2

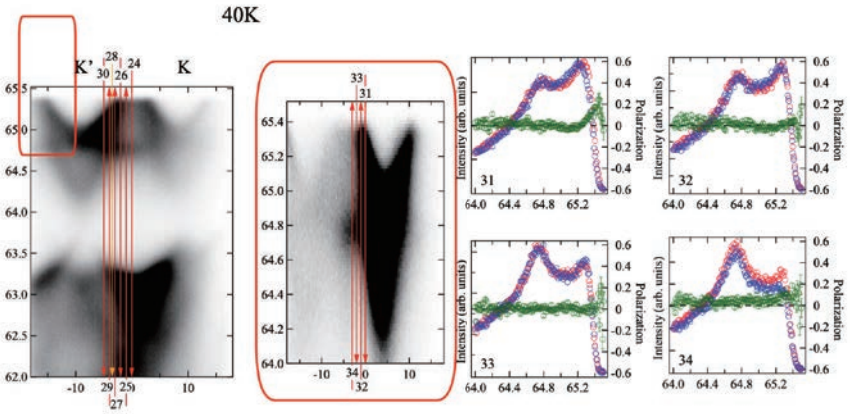

Fig. 5 Spin resolved data of the vally near K' of cut2

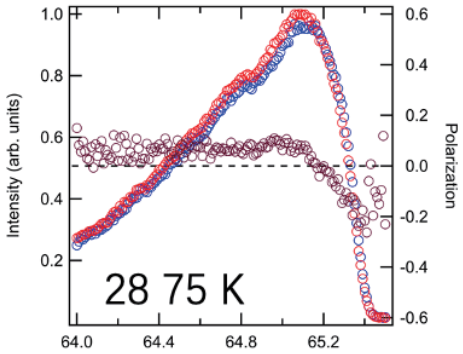

Fig. 6 spin polarization of line 28 at 75 K

[1] Hall, A.E., et al., *Magnetic structure investigation of the intercalated transition metal dichalcogenide V1/3NbS2.* Physical Review B, 2021. **103**(17).

[2] Lu, K., et al., *Canted antiferromagnetic order in the monoaxial chiral magnets V1/3TaS2 and V1/3NbS2.* Physical Review Materials, 2020. **4**(5).

[3] Smejkal, L., et al., *Crystal time-reversal symmetry breaking and spontaneous Hall effect in collinear antiferromagnets.* Sci Adv, 2020. **6**(23): p. eaaz8809.

[4] Šmejkal, L., J. Sinova, and T. Jungwirth, *Emerging Research Landscape of Altermagnetism.* Physical Review X, 2022. **12**(4).

[5] Šmejkal, L., J. Sinova, and T. Jungwirth, *Beyond Conventional Ferromagnetism and Antiferromagnetism: A Phase with Nonrelativistic Spin and Crystal Rotation Symmetry.* Physical Review X, 2022. **12**(3).

Chemical State Analysis of Titanium Oxide Powder Dispersed in Polymer by XAFS method

Susumu Mineoi[a], Kenjiro Momosaki[a], Hiroyuki Koga[b], Hirosuke Sumida[a]

[a]*Technical Research Center, Mazda Motor Corporation, 3-1 Shinchi, Fuchu-cho, Aki-Gun, Hiroshima 730-8670, Japan*
[b]*Advanced Automotive Research Collaborative Laboratory, Graduate School of Advanced Science and Engineering, Hiroshima University, 1-4-1 Kagamiyama, Higashi-Hiroshima, Hiroshima 739-8527, Japan*

Keywords: titanium oxide, powder sample, sample preparation, XAFS, XANES, pre-edge.

1. Introduction

X-ray Absorption Fine Structure (XAFS) is a powerful analytical method to clarify the chemical state of automotive materials such as battery materials, exhaust gas purification catalyst materials, rubber materials, metal materials and so on. So far, we have reported the results of deterioration analysis of automotive oils[1]. In the case of powder samples, it is necessary to prepare a sample having an appropriate optical thickness of $\Delta\mu t = 1$ in the energy range of target element. In the case of XAFS measurement in the soft X-ray range, even if boron nitride widely used in the hard X-ray region as a dilution matrix, absorption by boron nitride cannot be ignored, so it is difficult to prepare a sample having an appropriate optical thickness. There is also a method in which a powder sample is thinly applied to mending tape and a number of sheets are stacked, but measurement for adjustment is required for each sample to find an appropriate number of sheets. In this study, a sample preparation method for dispersing nano- and micro- size particle powder samples in a polymer matrix was investigated and the prepared samples were measured by transmission XAFS method.

2. Experimental

Powder samples used in this study were an anatase-type titanium dioxide powder (FUJIFILM Wako Pure Chemical Corporation), a rutile-type titanium dioxide powder (FUJIFILM Wako Pure Chemical Corporation) and a powder recovered from an amorphous titanium oxide nanoparticle dispersion (DAIHACHI CHEMICAL INDUSTRY CO., LTD.) by heating at 60 ~ 800 °C.

The powder dispersed polymer film samples were prepared by the following procedure. We mixed polyvinyl acetate emulsion (Konishi CO., Ltd.), deionized water and titanium oxide powder in a mass ratio of 5 : 5 : 1. As a mold for pouring the mixed solution, a hole with a diameter of 10 mm was punched into a 0.24mm thick polyvinyl chloride plate and mending tape was attached to one side. A predetermined amount of the mixed solution was poured into the prepared mold and cured to obtain analytical samples. The poured amount of mixed solution was adjusted so that $\Delta\mu t = 1$ in the titanium K-edge energy region.

Chemical state of titanium in each sample was investigated using XAFS measurement system at HiSOR BL11 with the transmission method. A sample was placed in an atmospheric gas filled sample chamber during the XAFS measurement. The XAFS spectra of the samples were acquired with the X-ray energy range from 4.900 to 5.090 keV. The interval value of 5 eV, 0.25 eV and 0.5 eV were applied to the energy range from 4.900 to 4.980 keV, from 4.980 to of 5.040 keV and from 5.040 to 5.090 keV, respectively. The incident X-ray energy was calibrated so that the highest intensity pre-edge peak energy of anatase-type titanium dioxide was 4.969 keV with reference to the literature [2], and the spectrum was measured with the transmission method. The XASF spectra were analyzed by using XAFS spectral analysis software Demeter (Athena) [3].

3. Results and discussion

Figure 1 shows appearance of powder dispersed polymer sample of this study. The sample is fixed to a copper sample holder for installation in the measurement chamber. The powder dispersed polymer sample can be self-supporting as a film even if it is removed from the mold of polyvinyl chloride plate and can be cut out to an appropriate size for XAFS measurement. In addition, samples of different sizes can be easily

prepared by the same procedure described in section 2.

Figure 2 shows titanium K-edge XANES spectra of the powder dispersed polymer samples. The shape of the spectrum was different from anatase-type, rutile-type and amorphous. It has been reported that titanium oxide has a different shape of K-edge energy range, because of the coordination state of atoms present around titanium and the valence of titanium atom [4][5]. The shape of pre-edge peak provides an indication of the structural and chemical state change of the titanium oxide. As the heat treatment temperature of the amorphous powder increased, the shape of pre-edge peak changed. The samples heat treated above 700 °C changed to an anatase-type titanium dioxide. It was found that the powder sample preparation method applied in this study was easy to use for achieving the appropriate optical thickness of the sample for XAFS measurement in the soft X-ray range.

The sample preparation method obtained in this study will also be used for X AFS analysis of other powder materials.

REFERENCES

1. S. Mineoi, K. Momosaki, H. Sumida, S. Hayakawa, HiSOR Activity Report 2021, 83(2022)
2. S. Matsuo, N. Sakaguchi, and H. Wakita, *Analytical Sciences* 21, 805–809 (2005)
3. B. Ravel and M. Newville, *Journal of Synchrotron Radiation* 12, 537-541 (2005)
4. F. Farges, G. E. Brown Jr, J. Rehr, *Geochimica et Cosmochimica Acta*, 60, 3023-3038 (1996)
5. T. Yamamoto, Adv. *X-Ray. Chem. Anal., Japan* 38, 45-65 (2007)

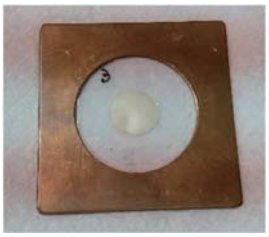

FIGURE 1. Appearance of powder dispersed polymer film sample.

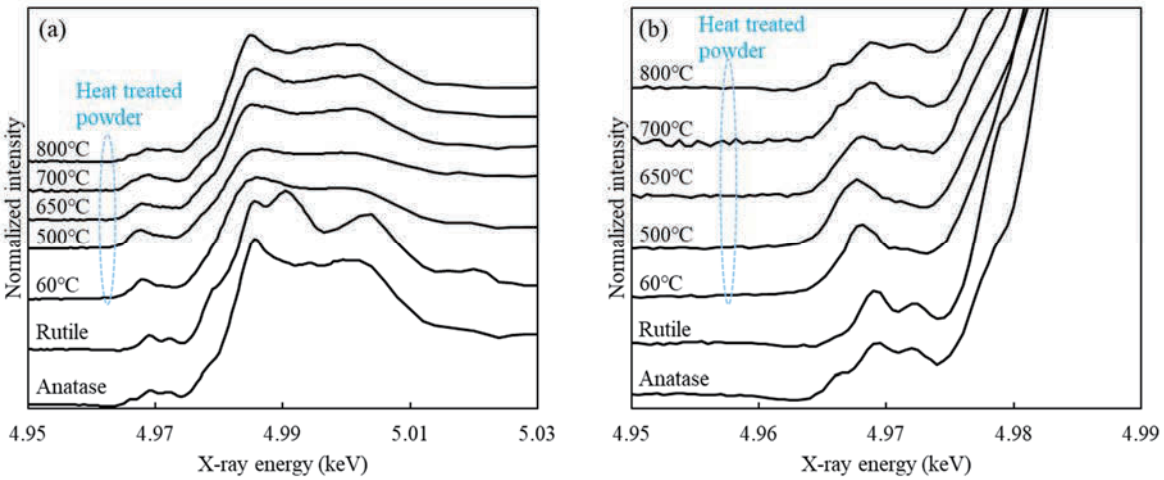

FIGURE 2. Titanium K-edge XANES(a) and pre-edge region (b) spectra of the titanium oxide dispersed polymer film samples.

VUV-CD Spectroscopy of Histone H2A-H2B Proteins Extracted from the Heated Cells

Yudai Izumi[a*], Koichi Matsuo[a], and Akinari Yokoya[b*]

[a]*Hiroshima Synchrotron Radiation Center (HiSOR), Hiroshima University, 2-313 Kagamiyama, Higashi-Hiroshima, Hiroshima 739-0046 Japan*
[b]*Institute for Quantum Life Science, Quantum Life and Medical Science Directorate, National Institutes for Quantum Science and Technology (QST), 2-4 Shirakata, Tokai, Ibaraki 319-1106, Japan*
**Present affiliation: Institute for Quantum Life Science, Quantum Life and Medical Science Directorate, National Institutes for Quantum Science and Technology (QST), 4-9-1 Anagawa, Inage-ku, Chiba 263-8555, Japan*

Keywords: Hyperthermia, radiosensitization, thermal denaturation, chromatin

1. Introduction

Heat exposure of cells in the temperature up to 45°C (hyperthermia) is one of the cancer treatments [1]. It is accepted that heat-induced DNA lesions and thermal denaturation of thermolabile proteins contribute to cell-death [2]. Differential scanning calorimetry (DSC) measurements revealed that histone proteins, building blocks of nucleosomes, are unfolded around 70°C–75°C in rodents and human cells [3]. On the other hand, circular dichroism (CD) spectroscopy, which reflects the contents of secondary structures of proteins, showed heating even below 65°C affects the structures of complex of histone H2A, H2B, H3, and H4 (core histone) proteins *in vitro* [4]. Another DSC [5] and CD [6, 7] measurements also reported that the denaturation of isolated H2A-H2B proteins progressed at the temperature region of hyperthermia and those were almost unfolded around 60°C. Although these contradictory reports imply that unidentified mechanisms prevent the thermal denaturation of histones *in vivo*, studies on the structural changes of histones in the heated cells have been scarce. In this study, we measured VUV-CD spectra of H2A-H2B proteins extracted from the heated cells (45°C for 3 h) to confirm the effects of cell heating on the histone structures.

2. Materials and methods

The detailed experimental procedure was described in our paper [8]. Briefly, the human cancer cells (HeLa.S-FUCCI cells) in the medium were heated in air at 45°C for 3 h. H2A-H2B was extracted from the heated cells immediately or after 2-h incubation at 37°C. For comparison, H2A-H2B was also extracted from the cells placed in air at 37°C for 3 h. The extracted H2A-H2B was dissolved in 10-mM Tris-HCl buffer supplemented with 250-mM NaF (pH 8.5).

VUV-CD spectroscopy was performed in the BL-12 at the Hiroshima Synchrotron Radiation Center (HiSOR) in Japan [9]. The path length of the sample cell was 50 μm. The CD spectra were analyzed to determine the secondary structure contents of H2A-H2B using the BeStSel program [10, 11]

3. Results and Discussion

Figure 1 shows CD spectra of the H2A-H2B extracted from the heated cells measured at 25°C. CD spectra of the H2A-H2B extracted from the unheated cells measured at 25 and 45°C are also shown in Fig. 1 for comparison. The error bars represent the standard deviation. The H2A-H2B extracted from the unheated cells (control sample) exhibited a positive peak at around 190 nm and two negative peaks at around 208 and 222 nm at 25°C. Heating the control sample up to 45°C, absolute values of peak intensities decreased and the peaks shifted toward the shorter wavelength region. Those spectral changes are characteristics of typical thermal denaturation of α-helix rich proteins. For the H2A-H2B extracted immediately from the heated cells (45-0 sample) measured at 25°C, the absolute values of the CD peak intensities were larger than those of the control sample measured at 25°C. The H2A-H2B extracted from the heated cells after 2-h incubation (45-2 sample), demonstrated that the CD spectrum was correctly matched with that of the control sample measured at 25°C within the error range. Thus, the spectral changes observed in the 45-0 and 45-2 samples differed

from those of the H2A-H2B thermally denatured *in vitro*.

The secondary structure contents of the control, 45-0, and 45-2 samples are listed in Table 1. For the control sample measured at 45°C, the content of α-helices decreased but those of β-strand and other structures increased compared to those contents at 25°C. On the other hand, for the 45-0 sample, the secondary structure content of α-helices increased, but those of β-strands and turns decreased compared with the contents of the control sample at 25°C. The contents of the 45-2 sample agreed well with those of the control sample within the error range. Hence, structural alterations of H2A-H2B induced in the cells heated at 45°C for 3h differed from those induced *in vitro*. The altered structures were gradually recovered within 2 h in the 45°C-heated cells.

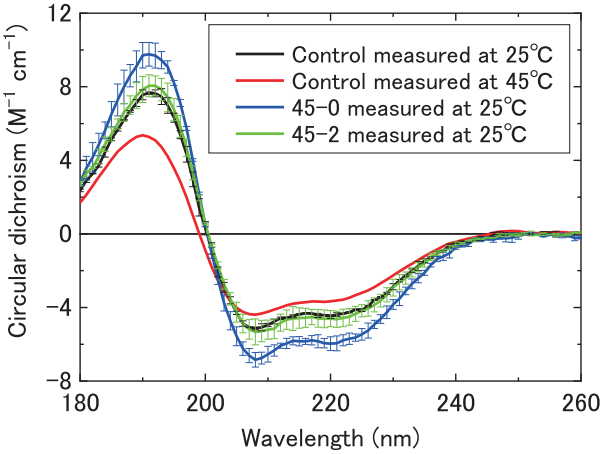

FIGURE 1. CD spectra of the H2A-H2B extracted from the unheated and heated cells measured at 25 and 45°C.

TABLE 1. The secondary structure contents (%) of H2A-H2B extracted from the unheated and heated cells at 25 and 45°C.

	Control at 25°C	**Control at 45°C**	**45-0 at 25°C**	**45-2 at 25°C**
α-Helix	39.9±1.9	28.8	52.0±1.4	44.3±3.0
β-Strand	10.3±1.8	20.8	1.1(+1.5/−1.1)	5.3±0.4
Turn	13.3±0.1	12.6	9.2±0.4	13.7±2.0
Others	36.6±1.0	37.8	37.6±0.6	34.5±0.2

4. Conclusions

Heat stress (45°C for 3 h) induced structural alterations in histone H2A-H2B proteins in cells. The secondary structure content of α-helices increased but that of β-strands decreased. Those changes differed from the ordinary thermal denaturation observed in the directly heated H2A-H2B. The underlying mechanisms and roles of the structural changes have yet been unidentified. However, the structural alterations of H2A-H2B might be induced by cellular functions to resist heat-induced DNA lesions, such as DNA damage repair pathways because similar structural alterations were observed in H2A-H2B extracted from X-ray irradiated cells [12].

Acknowledgments

This work was financially supported by JSPS KAKENHI Grant Numbers JP17K12825 and JP20K12164.

REFERENCES

[1] B. K. Bhuyan et al., Cancer Res. 39, 2277-2284 (1979). [2] J. L. Roti Roti, Int. J. Hyperthermia 24, 3-15 (2008). [3] J. R. Lepock, Methods 35, 117-125 (2005). [4] F. X. Wilhelm et al., Eur. J. Biochem. 45, 431-443 (1974). [5] W. O. Weischer et al., Nucleic Acids Res. 5, 139-160 (1978). [6] V. Karantza et al., Biochem. 34, 5988-5996 (1995). [7] Y. Izumi et al., Biophys. J. 111, 69-78 (2016). [8] Y. Izumi et al., Chirality 35, 165-171 (2023). [9] K. Matsuo and K. Gekko, Bull. Chem. Soc. Jpn. 86, 675-689 (2013). [10] A. Micsonai et al., Proc. Natl. Acad. Sci. USA 112, E3095-E3103 (2015). [11] A. Micsonai et al., Nucleic Acids Res. 46, W315-W322 (2018). [12] Y. Izumi, Quantum Beam Sci. 3, 23 (2019).

Molecular crowding effect on the RecA/DNA interactions

Raeyeong Kim[a], Kentaro Ito[b], Seog K. Kim[a], Koichi Matsuo[c] and Masayuki Takahashi[b],

[a] *Department of Chemistry, Yeungnam University, 280 Daehak-ro, Gyeongsan-city 38541, South Korea*
[b] *School of Life Science and Technology, Tokyo Institute of Technology, 2-12-1Ookayama, Meguro-ku, Tokyo 152-8550, Japan*
[c] *Hiroshima Synchrotron Radiation Center, Hiroshima University, 1-3-1 Kagam iyama, Higashi-Hiroshima 739-8526, Japan*

Keywords: RecA protein, DNA strand exchange, homologous recombination, linear dichroism, molecular crowding.

RecA recombinase catalyzes strand exchange between two DNA with the same sequence for homologous recombination. RecA is thus involved in the repair of double strand break, the most severe DNA damage, and regression of stalled replication fork [1, 2]. Similar proteins exist in all living organisms.

RecA binds first to the single-stranded part of DNA for the reaction and forms a helical filament around the DNA [1, 2]. RecA then binds double-stranded DNA (dsDNA) with a similar sequence to the single-stranded DNA (ssDNA) and performs a strand exchange reaction in the presence of ATP [1, 2]. Purified RecA can perform the reaction in vitro. However, the reaction speed, especially the binding of dsDNA, is slow. The reaction in vivo may be activated by other protein factors and the environment [1, 2]. We examined whether crowing environment affects the DNA binding of RecA by examing the effect of crowding mimic agents, polyethyleneglycole (PEG) and in vitro.

The binding of RecA to ssDNA and dsDNA is investigated by measuring the fluorescence anisotropy of the fluorescent probe attached to oligonucleotides. RecA binding stiffens DNA and increases the fluorescence anisotropy. The binding to poly(dT), typical ssDNA without any secondary structure, was not affected by po

changes in linear dichroism signal. LD measures the absorption difference of differently polarized light beams on aligned samples. Biding RecA stiffens DNA and strongly increases LD signal intensity (ref).

If you start a new paragraph, please use “Enter” or "Return" key on your keyboard. The indent is automatically inserted at the start of this paragraph.
If you want to make a line feed without indent, we can enter “Shift + Enter” keys. This is the result of the procedure.

Reference number should be shown using brackets like [1]. If you want to refer to several references, you can do it like [1, 2] or [3-5].

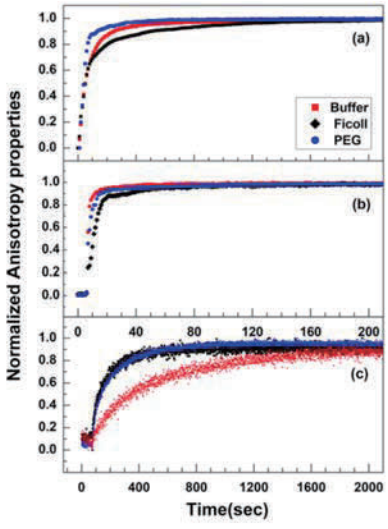

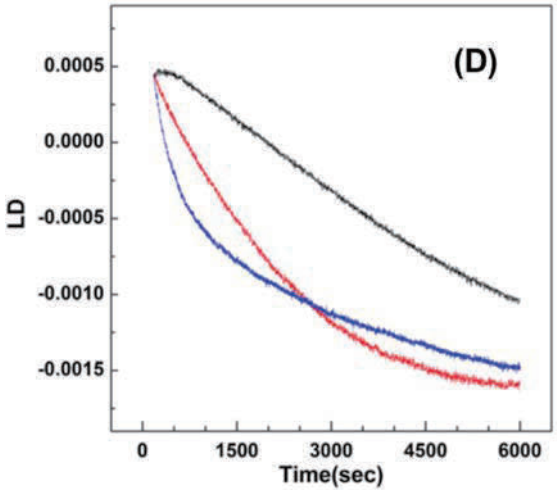

FIGURE 1. This is a style of figure caption. The font size is 9 pt. The figure is centered as shown above. The plots in this figure are calculated from eq. 1 [6].

The main text continues from here. Below is an example of Table. The table format is described in the caption.

TABLE 1. This is the style of Table captions. Font size is 9 pt. Column titles are capitalized for each letter and bold-font. Row names are capitalized for each letter and left-justified. Contents are centered.

Column Title	**Column Title**	**Column Title**
Row Name	x	y
Row Name	x	y
Row Name	x	y

Below is an example equation created with Office built-in equations. To make numbering of the equation, the table tool is used with a setting of “No Border”. The equation is centered in the column, and the number is righted. This equation shows a spectral function of the synchrotron radiation for a short bending magnet [6]. In the "paragraph" setting use 6pt spacing above and below the equation.

$$S\left(\frac{\omega}{\omega_c}\right) = \frac{9\sqrt{3}\omega}{8\pi\omega_c}\int_{\omega/\omega_c}^{\infty} K_{5/3}(z')dz'. \tag{1}$$

If you do not use the numbering of equations, you can just enter the equation like:

$$S\left(\frac{\omega}{\omega_c}\right) = \frac{9\sqrt{3}\omega}{8\pi\omega_c}\int_{\omega/\omega_c}^{\infty} K_{5/3}(z')dz'.$$

The equation is automatically centered in this case.
You can also put an equation in the main text like, $\gamma\beta - \alpha^2 = 1$.

REFERENCES

1. P Howard-Flanders, S C West, A Stasiak (1984) Nature 309: 215-219.
2. Shibata, T., DasGupta, C., Cunningham, R. P., & Radding, C. M. (1979). Proc. Natl. Acad. Sci. USA, 76(4), 1638-1642.
2. Norden B, Elvingson C, Kubista M, Sjöberg B, Ryberg H, Ryberg M, Mortensen K & Takahashi M (1992) J. Mol. Biol. 226, 1175-1191.
5. I. J. David, "Effects of Sugars on Tea and Coffee", Ph.D. Thesis, Hiroshima University, 1942.
6. A. Hofmann, “Characteristics of Synchrotron Radiation” in Proceedings of CERN Accelerator School, edited by S. Turner, CERN 98-04, CERN, Genève, 1998, pp. 1-44.

Secondary Structural Changes in FUS-LC causing Liquid-Liquid Phase Separation

Kentaro Fujii[a], Nobuo Maita[a], Koichi Matsuo[b], and Masato Kato[a]

[a]*Institute for Quantum Life Science, National Institutes for Quantum Science and Technology, 4-9-1 Anagawa, Inage-ku, Chiba-city, Chiba, 263-8555 JAPAN*

[b]*Hiroshima Synchrotron Radiation Center, Hiroshima-university, 2-313 Kagamiyama, Higashihiroshima-city, Hiroshima, 739-0046 JAPAN*

Keywords: Liquid-Liquid Phase Separation, FUS-LC, VUV-CD

Aggregation of the RNA-binding protein FUS (Fused in Sarcoma) has been implicated in neurodegenerative diseases such as ALS (amyotrophic lateral sclerosis) and FTD (frontotemporal dementia). The low-complexity domain of the FUS (FUS-LC) mediated liquid-liquid phase separation (LLPS), but the structural mechanism is not known in detail. To address the revealing mechanism, we examined the spectroscopic study using VUV-CD measurement, which can analyze the secondary structure of the proteins.

CD measurements were performed at BL12 VUV-CD station in HiSOR. CD spectra were measured between 185 and 260 nm. The temperature of the samples was controlled from room temperature to 5°C to obtain the LLPS of the FUS LC.

The CD spectrum obtained by measuring at room temperature has a prominent peak at 195 nm and a small shoulder peak near 220 nm. This shows that the major structure is a random coil since the spectrum was similar to that of STI, which is mainly an unordered structure. This result is consistent with that obtained from NMR measurement.

The peak intensity of this CD spectrum may change on the order of tens of minutes after sample preparation. Since obtaining data to analyze this change over time with the given beam time is difficult, we embarked on an experiment to track the difference in the CD spectrum over time using an in-house CD spectrometer.

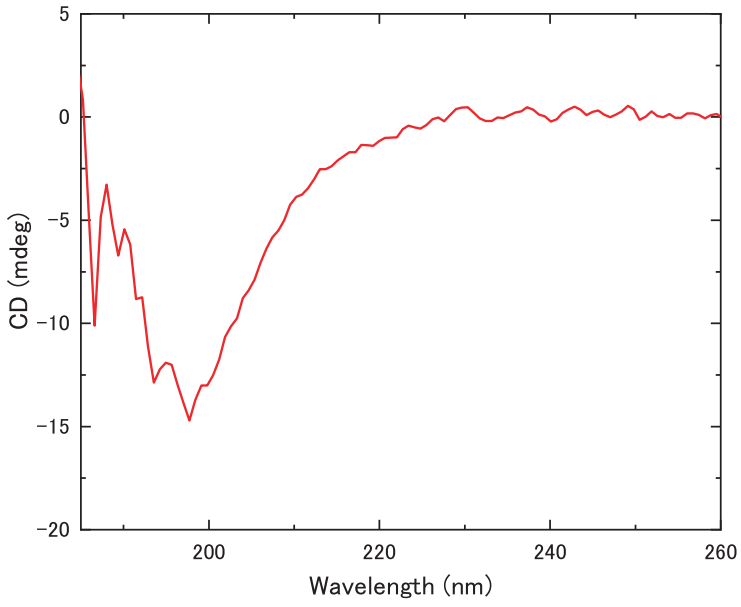

FIGURE 1. The obtained VUV-CD spectrum of FUS-LC.

REFERENCES

1. M. Nolan, K. Talbot, O. Ansorge, *Acta. Neuropathologica Communications* **4** (2016) 99.

2. M. Sawada, H. Namatame, M. Taniguchi, *J. Phys. Conf. Ser.* **425** (2013) 162010.

Secondary Structure Content of Strawberry Allergen Fra a 1 Treated at Different Temperatures

Y. Ueyama[a], K. Matsuo[b], M. Nishino[c], K. Noda[d], M. Ishibashi[e,f], Y. Uno[e] and Y. Nitta[d]

[a] *Department of Nutrition and Food Science, Ochanomizu university, Tokyo, 112-8610, Japan*
[b] *Hiroshima Synchrotron Radiation Center, Hiroshima university, Hiroshima, 739-0046, Japan*
[c] *Graduate school of Humanities and Sciences, Ochanomizu university, Tokyo, 112-8610, Japan*
[d] *Natural Science Division, Ochanomizu University, Tokyo, 112-8610, Japan*
[e] *Graduate School of Agricultural Science, Kobe university, Hyogo, 657-8501, Japan*
[f] *Graduate School of Agriculture, Kyoto university, Kyoto, 606-8501, Japan*

Keywords: Oral allergy syndrome, Pollen-food allergy syndrome, NMR, HSQC spectra

Strawberries contain an allergen that is associated with oral allergic syndrome (OAS), also known as pollen food allergy syndrome. Fra a 1 is one of the major allergens in strawberries [1] and might decrease their allergenicity by heating, likely due to structural changes in the allergen leading to decreased recognition of the allergens in the oral cavity. In the present study change in the secondary structure content of Fra a 1 isoforms, Fra a 1.01 and Fra a 1.02, was investigated by treating at different thermal histories.

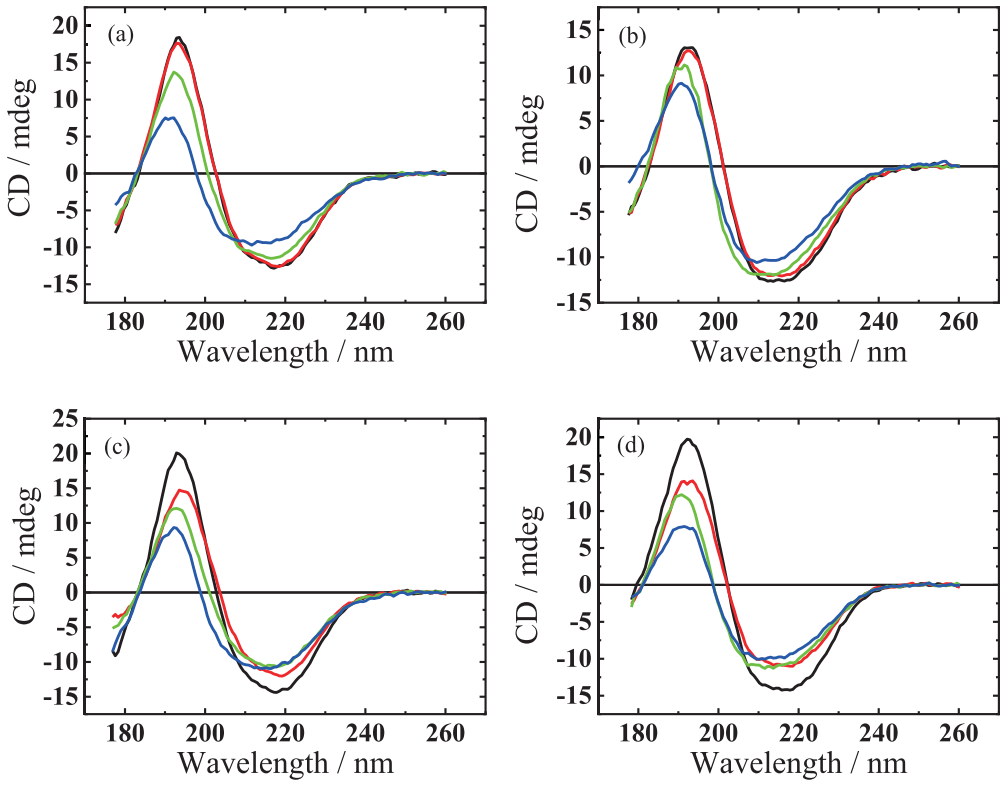

FIGURE 1. VUVCD spectra for (a) Fra a 1.01 and (b) Fra a 1.02 in 20 mM Na phosphate buffer (pH 7.4) with 1mM mercaptoethanol, (c) Fra a 1.01 and (d) Fra a 1.02 in 20 mM Na phosphate buffer (pH 7.4) with 5mM TCEP. Samples were measured at 25 ℃ without heating (black line) or after heating to 40 ℃ (red line), 60 ℃ (green line) and 80 ℃ (blue line).

Recombinant Fra a 1.01 and Fra a 1.02 were prepared by *E. coli* expression system. To avoid aggregation due to disulfide bonding, mercaptoethanol or tris(2-carboxyethyl)phosphine (TCEP) was added into sample solutions. Vacuum-ultra circular dichroism (VUVCD) experiment was performed at 25 ℃ for the samples without heating and for the samples heated to 40 ℃, 60 ℃ and 80 ℃ and then cooled to 25 ℃.

From VUVCD spectra for each sample (Fig.1), the secondary structure content was estimated. As shown in Table 1, only the secondary structure content of Fra a 1.01 was estimated. Fra a 1.02 failed to be estimated, probably because the relationship between the CD intensity and the spectral shape was different from that of normal proteins. According to ^{1}H-^{15}N HSQC spectra of NMR experiments [2], heating above 60 ℃ caused thermally denaturation of Fra a 1.02. It is inferred that the secondary structure content could not be estimated from the Fra a 1.02 structure after heat denaturation. On the other hand, the HSQC spectrum of Fra a 1.01 did not clearly show thermal denaturation after heating above 60 ℃ [2]. Although the shape of the spectrum of the Fra a 1.01 sample after heating over 60 ℃ changed compared to that of the sample without heating (Fig.1), the secondary structure content could be estimated. It was suggested that structural changes due to heat treatment occurred only in limited regions of Fra a 1.01.

TABLE 1. Estimated secondary structure content of Fra a 1.01 with mercaptoethanol or TCEP.

		Helix	Sheet	Turn	Random
Fra a 1.01 with mercaptoethanol	25 ℃	16	32	23	29
	40→25 ℃	16	31	23	29
	60→25 ℃	8	42	22	28
	80→25 ℃	9	37	21	33
Fra a 1.01 with TCEP	25 ℃	22	28	23	28
	40→25 ℃	18	31	23	29
	60→25 ℃	17	29	22	32
	80→25 ℃	15	29	22	34

REFERENCES

1. M. Ishibashi, T. Nabe, Y. Nitta, H. Tsuruta, M. Iduhara, and Y. Uno, *Plant Cell Rep*., **37**, 411–424 (2018).
2. M. Nishino, K. Noda, M. Ishibashi, Y. Uno, and Y. Nitta *Protein Expr. Purif*., **210**, 106296 (2023).

Synchrotron Radiation Circular Dichroism Study of Exopolysaccharides from Marine Resources

Mohamed I. A. Ibrahim[a, b*], Hassan A.H. Ibrahim [b], Tatsuki Haga[a], Koichi Matsuo[a] Ahmed M. Gad[b]

[a]*Hiroshima Synchrotron Radiation Center, Hiroshima University, 2-313 Kagamiyama, Higashi-Hiroshima, Hiroshima 739-0046, Japan.*
[b]*National Institute of Oceanography and Fisheries (NIOF), Cairo, Egypt.*

Keywords: Exopolysaccharide; *Aspergillus oryzae;* Helix-like Conformation; Circular Dichroism.

Polysaccharides are ubiquitous in nature derived from different sources such as seaweed, plants, animals, and microorganisms (e.g., bacteria and fungi). Microbial polysaccharides exhibit unique molecular structures that allow them as promising candidates in versatile applications [1-2]. Fungal polysaccharides and particularly extracellular polysaccharides (EPS) have extra advantages over the intracellular and cell wall polysaccharide due to their high production yield using a straightforward separation and purification processes [3]. The EPS and specifically marine fungal EPS have been applied in biomedical applications as antioxidant, anti-inflammatory, anticoagulant, wound dressing, etc. agents [1-5].

In this study, various physicochemical techniques and methods were applied to investigate the structure and conformation features of EPS produced by *Aspergillus oryzae* strain Gad7. First, seven fungal strains were obtained from different bacteria samples collected along the Alexandria coast of the Egyptian Mediterranean Sea in 2021. Then, all the strains were screened for EPS production grown on seawater Sabouraud Dextrose broth medium at 30 ± 0.2°C and pH 5.0 ± 0.1 for 6 days on a static incubator. The results showed that the AG7 isolate was the most potent EPS producer of ~ 5.19 ± 0.017 g L^{-1} yield and was identified morphologically and genetically by using 18S rDNA as *Aspergillus oryzae* strain Gad7.

The UV-Vis analysis revealed the efficient extraction and purification steps of the EPS-AG7 with a high carbohydrate content of 87.5%, and the technique determined the sulphate percentage of 24%. The sulphated nature of the EPS-AG7 was also confirmed by the FTIR study by the stretching vibration of the S=O at ύ = 1185 – 1250 cm^{-1} (data not shown). Size exclusion chromatography (SEC) analysis investigated that the EPS-AG7 was a homogenous polysaccharide with an average molecular weight ($\overline{Mw}$) of ~ 7.34 kDa. HPLC analysis indicated that the EPS-AG7 was a heterogeneous polysaccharide composed of mannose: glucose: arabinose: galacturonic acid: galactose: lyxose at a molar ratio of 6.6 : 3.9 : 1.8 : 1.3 : 1.1 : 1.0, respectively. The molecular structure of the EPS-AG7 could not be solved by NMR technique due to structure complexity; however, the ^{1}H NMR identified that the monosaccharides are linked together through α- and β-glycosidic linkages (data not shown).

Additionally, UV-Vis technique through the Congo Red experiment investigated that EPS-AG7 adopted triple-helix like conformation which was confirmed by circular dichroism (CD) studies (data not shown). Furthermore, the synchrotron radiation circular dichroism (SRCD) data suggested that the EPS-AG7 adopted a helical-like arrangement in both water (Figure 1) and Tris-HCl buffer and the structure was not disturbed under different experimental conditions such as concentration, temperature, ionic strength (data not shown). Additionally, the CD data revealed the stability of the helix-like structure in the presence of different lipid liposomes including (DOPC, DOPE, and DOPS) without any conformational change of the EPS-AG7 (data not shown).

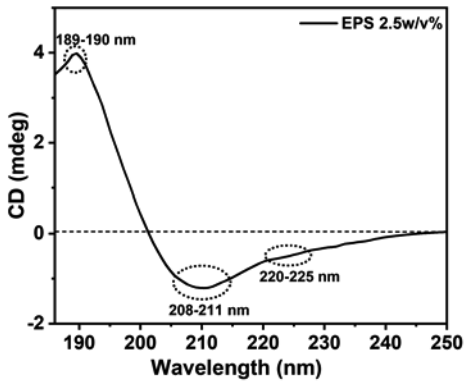

FIGURE 1. The VUV-CD spectrum of EPS-AG7 by *Aspergillus oryzae* GAD7 (2.5 w/v% in DW at 25°C).

REFERENCES

1. W. Wang, et al., Food Chem.: X, 2022. 15: p. 100414.
2. N. Suryawanshi, Naik S., and S.E. Jujjawarapu, Food Sci. Appl. Biotechnol., 2022(1): p. 22-44.
3. M. Hamidi, et al., Carbohydr. Polym., 2022. 284: p. 119152.
4. S. Mahapatra, and D. Banerjee, Microbiol. Insights, 2013. 6: p. 1-16.
5. L. Mo, et al., Int. J. Biol. Macromol., 2017. 95: p. 385-392.

Hydration Structure of Acetone Studied with Concentration-Dependent Absorption Spectra in the Ultraviolet Region

Chika Sugahara[a], Koichi Matsuo[b], and Kazumasa Okada[a,b]

[a] *Graduate School of Advanced Science and Engineering, Hiroshima University, 1-3-1 Kagamiyama, Higashi-Hiroshima 739-8526, Japan*
[b] *Hiroshima Synchrotron Radiation Center, Hiroshima University, 2-313 Kagamiyama, Higashi-Hiroshima 739-0046, Japan*

Keywords: UV absorption spectra, chemometric analysis, hydration structure

Hydration structure plays a fundamental role in our understanding of physical properties and chemical reactions of solutes. One of the typical aqueous solutions is acetone solution, but the physicochemical properties still need to be studied. Acetone is miscible with water in any ratio. The mixture has a negative excess enthalpy in the dilute region [1], indicating an attractive interaction between acetone and water. The interaction is a hydrogen-bond type, with an additional weak C–H···O bond in a very dilute region [2]. The purpose of this study is to explore the hydration structure of acetone using UV absorption spectroscopy.

The experiments were performed on the beamline for vacuum-ultraviolet circular dichroism spectroscopy, BL-12. The sample chamber [3] was filled with the nitrogen gas. The sample cell consisted of two CaF_2 windows and a Teflon spacer with a thickness of 200 μm. The measurement range was 170–320 nm, and the spectrum of liquid water was used as a reference. The sample acetone–water binary mixture was prepared with molar fraction of acetone ranging from 0.05 to 0.50. Acetone was obtained commercially from FUJIFILM Wako Pure Chemicals Corp., Japan.

The peak of $\pi^* \leftarrow n$ absorption band non-linearly shifts to the longer wavelength with the molar fraction of acetone, x_A. The absorption band and the peak shift are shown in Fig. 1. All the spectra have a tail toward the shorter wavelength. This implies that the spectra consist of some components. The components include hydrated acetone. The hydration structure depends on x_A. Judging from the shift of the peak position, there are three regions: Region 1; $x_A =$ 0.05–0.10; Region 2, $x_A =$ 0.15–0.35; and Region 3, $x_A =$ 0.40–0.50.

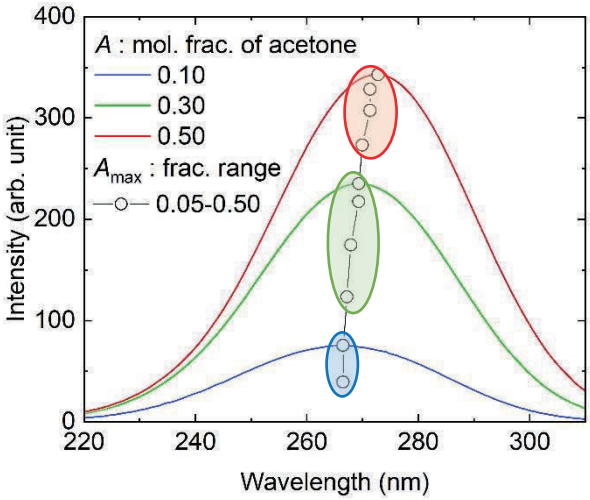

FIGURE 1. The $\pi^* \leftarrow n$ absorption band of acetone aqueous solution at different molar fractions.

Quantitative analysis of the change of the band has been carried out by the principle component analysis (PCA). The result of PCA is shown in Fig. 2. The measurement spectra are well explained by two components (total 99.99%). The primary component (PC1) has a peak at 270.70 nm and the secondary component (PC2) has a peak at 252.64 nm and a valley at 287.36 nm. The vector of PC1 corresponds to the average spectrum, and the score of PC1 is almost proportional to x_A. The score of PC2 increases in $x_A = 0.05$–0.20, reduces in $x_A = 0.25$–0.35, and is negative in $x_A = 0.40$–0.50. The PC1 is similar to the spectrum for $x_A = 0.35$. This indicates that the dominant hydration structure is the 1:1 acetone–water complex. Additional hydration structures are analyzed as PC2.

The physical meaning of PC2 is made clearer if we plot the difference spectra from PC1. The difference spectra have a sinusoidal-like shape. The behavior of peak shift is reproduced by the difference spectra. Peaks come at shorter wavelengths in the spectra for Region 1, suggesting an additional attractive interaction with water. A possible interaction model is shown in Fig. 3(a): The acetone molecule interacts with two water molecules. This kind of hydration model is the same as that proposed in an IR and NMR spectroscopic study [2]. In Region 2, two acetone molecules are hydrated with one water molecule like in Fig. 3(b). In Region 3, there are not enough water molecules for hydration due to the large x_A: The solution contains non-hydrogen-bonded acetone molecules. The presence of the non-hydrogen-bonded molecules is supported by the coincidence of the peak of PC2 with the absorption peak position of gaseous acetone [4].

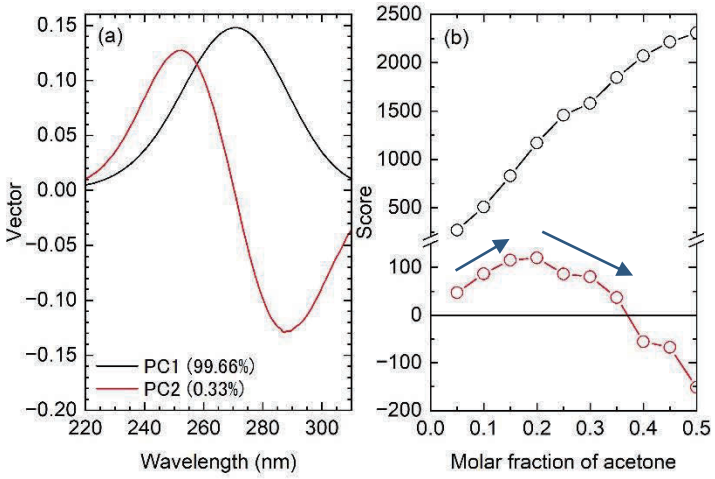

FIGURE 2. Spectral components (a) and scores (b) obtained by PCA for the UV absorption data presented in Fig. 1.

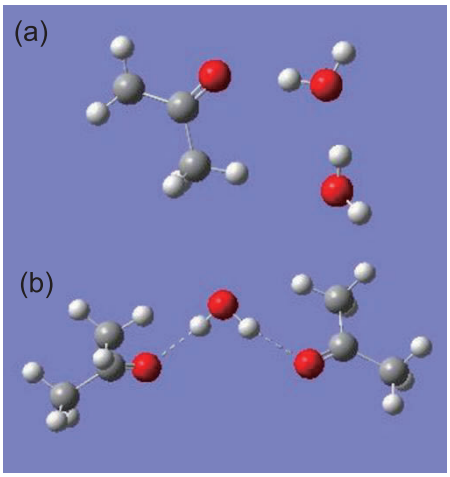

FIGURE 3. Plausible hydration structures of acetone; (a) 1:2 complex, (b) 2:1 complex.

REFERENCES

1. B. Löwen and S. Schultz, *Thermochim. Acta* **262**, 69–82 (1995).
2. K. Mizuno, T. Ochi, and Y. Shindo, *J. Chem. Phys.* **109**, 9502–9507 (1998).
3. K. Matsuo, T. Fukuyama, R. Yonehara, H. Namatame, M. Taniguchi, and K. Gekko, *J. Electron Spectrosc. Relat. Phenom.* **144–147**, 1023–1025 (2005).
4. M. Nobre, A. Fernandes, F. Ferreira da Silva, R. Antunes, D. Almeida, V. Kokhan, S. V. Hoffmann, N. J. Mason, S. Eden, and P. Limão-Vieira, *Phys. Chem. Chem. Phys.*, **10**, 550–560 (2008).

Optical Activity Measurement of Amino-acid Films Irradiated with Circularly Polarized Lyman-α Light

Jun-ichi Takahashi[a], Masahiro Kobayashi[b], Gen Fujimori[a], Kensei Kobayashi[a]
Hiroshi Ota[c], Koichi Matsuo[d], Masahiro Katoh[c,d], Yoko Kebukawa[a]
Shinji Yoshimura[b], Hiroaki Nakamura[b]

[a]*Faculty of Engineering, Yokohama National University, 79-5 Tokiwadai, Hodogaya-ku, Yokohama 240-8501, Japan*
[b]*Department of Helical Plasma Research, National Institute for Fusion Science, 322-6 Oroshi-cho, Toki 509-5292, Japan*
[c]*UVSOR Facility, Institute for Molecular Science, 38 Nishigo-Naka, Myodaiji, Okazaki 444-8585, Japan*
[d]*Hiroshima Synchrotron Radiation Center, Hiroshima University, 2-313 Kagamiyama, Higashi-Hiroshima 739-0046, Japan*

Keywords: Homochirality, Amino Acid, Optical Activity, Circularly Polarized Light, Circular Dichroism.

The origin of homochirality in terrestrial biomolecules (L-amino acid and D-sugar dominant) remains one of the most mysterious problems in the research for the origins of life. Rational explanations for the chiral asymmetry introduction into biomolecules are required through interdisciplinary collaborations. One of the most attractive hypotheses in the context of astrobiology is “Cosmic Scenario” as below [1, 2]; (1) Asymmetric reactions of prebiotic molecules on interstellar dust surfaces in molecular cloud circumstances were introduced by polarized quantum radiation sources in space, that is “chiral radiations”. (2) The chiral products were transformed into the complex organic materials including amino-acid precursors as “chiral seeds”. (3) The complex organic materials as “chiral seeds” were transported with meteorites or asteroids to primitive Earth and resulting in terrestrial biomolecular homochirality by some “chiral amplification” effect.

Among the polarized quantum radiation sources, circularly polarized light (CPL) in the space environment is thought to be one of the most likely causes of the enantiomeric excesses of terrestrial bioorganic molecules. A cosmogenic scenario has attracted attention, which proposes that the radiation fields of CPL induce new optical activity in organic molecules produced in the interstellar environment, leading to the enantiomeric excesses. The radiation fields of CPL are assumed to exist in the scattered light by magnetic field-aligned dust in massive star-forming regions [3] and in synchrotron radiation (SR) or gamma-ray bursts from neutron stars with strong magnetic fields [2]. Ultraviolet light with a wavelength shorter than 230 nm is highly absorbed by bioorganic molecules such as amino acids. Furthermore, this is in the region where the optical response to left- (L-) and right- (R-) CPL is of opposite sign, that is, optical activity is prominent.

To validate the cosmogenic scenario, several ground simulating experiments have been investigated using ultraviolet CPL from high-energy particle accelerators. We have already carried out irradiation experiments of ultraviolet CPL with different wavelengths (215, 180 and 155 nm) to investigate the photon energy dependence of chiral asymmetric reactions by using UVSOR beam lines [4, 5]. Photon absorption bands correspond with the chromophores from the characteristic electronic transitions of carboxyl and amino groups (n-π*, π-π* and n-σ*, respectively) of alanine molecule [6, 7]. The results of circular dichroism (CD) measurements strongly suggested that optical activity emergence depends on photon energy of the irradiated CPL.

In this study, we focused on a hydrogen Lyman-α wavelength of 121.6 nm, where strong emission lines are observed in star-forming regions. Furthermore, it is predicted by recent theoretical calculations that the hydrogen Lyman-α light is circularly polarized by the magnetic field-aligned dust scattering in massive star-forming regions. We have carried out irradiation experiments by using circularly polarized hydrogen Lyman-α light to investigate the further photon energy dependence of chiral asymmetric reactions. We formed thin solid film samples of racemic mixture of alanine (DL-alanine) on quartz substrates from crystal powders of

DL-alanine by using a thermal-crucible vacuum-evaporation system. The samples were irradiated with L- or R-CPL in hydrogen Lyman-α wavelength of 121.6 nm using the undulator beam line BL1U of UVSOR-III. The irradiated CPL wavelength are corresponding to photon absorption bands with the chromophores from the electronic transitions of carboxyl and amino groups (π -σ*) of alanine molecule [6, 7]. The samples were set in a vacuum sample chamber preventing attenuation by air absorption. The 121.6 nm wavelength radiation from the undulator is reflected by a gold-coated mirror located in the mirror chamber directly beam upstream of the sample chamber and then enters the sample chamber. On the beam entrance side of the vacuum sample chamber, a gate valve with an MgF_2 vacuum sealing window (0.5 mm in thickness) was mounted. The use of gold-coated mirror reflections has made it possible to suppress high-energy higher-order light from the undulator source expecting to reduce the transmittance loss of the MgF_2 window due to high-energy radiation induced defects. The sample substrate was set in the sample holder, in which magnetic and electric fields can be applied to perpendicularly to the sample surface. The total photon beam intensity irradiated on the sample was monitored with photoelectron current of a silicon photodiode settled at the beam downstream side of the sample holder.

CD spectra of the CPL irradiated films were measured using the SR-CD beam line BL-12 of HiSOR to clarify the optical activity emergence by CPL irradiation. CD spectroscopy can detect optical activity with a high accuracy because CD spectra sensitively reflects the steric structures of chiral molecules. Figure 1(a) shows spectra of DL-alanine films irradiated for 30 min with L- or R-CPL at 121.6 nm in wavelength. To delete the effects of linear dichroism components, the CD spectra at sample rotation angles (0, 45, 90, and 135 degrees) from both back and front directions of each were individually measured and averaged them. Comparing with CD spectra of irradiations at 215, 180 and 155 nm in wavelength, the observed optical activity emergence strongly depends on the irradiated CPL wavelength and the polarization helicity (L- or R-CPL). In addition, we have also examined the additional effect of applying a magnetic field to the sample to investigate the effect of the magnetic field in interstellar space (Fig. 1(b) and (c)). Detailed analysis of CD spectra is in progress supported by quantum chemical calculations. The clarification of full mechanism of the optical activity emergence potentially has relevance to the origin of terrestrial bioorganic homochirality stimulated by “chiral photon radiation”.

This work is supported by the Astrobiology Center Program of National Institutes of Natural Sciences (NINS) (Grant Number AB041014) and Frontier Photonic Sciences Project of National Institutes of Natural Sciences (NINS) (Grant Number 01212202).

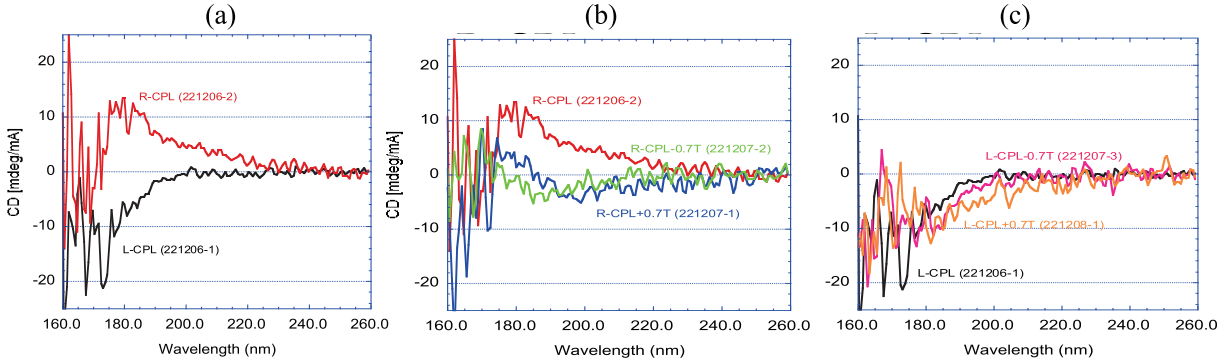

FIGURE 1. (a) CD spectra after right (R-) and left (L-) circularly polarized Lyman-α (121.6 nm) irradiation on DL-alanine films without magnetic field, (b) right (R-) circularly polarized Lyman-α irradiation with magnetic field (±0.7 T), and (c) left (L-) circularly polarized Lyman-α irradiation with magnetic field (±0.7 T).

REFERENCES

1. W. A. Bonner, *Orig. Life Evol. Biosph.* **21**, 407 (1991).
2. J. Takahashi and K. Kobayashi, *Symmetry* **11**, 919 (2019).
3. H. Fukushima, et al., *Month. Notices Roy. Astron. Soc.* **496** 2762 (2020).
4. J. Takahashi et al., *Int. J. Mol. Sci.* **10**, 3044 (2009).
5. T. Sakamoto et al., in Proceedings of 25th Hiroshima Int. Conf. Synchrotron Radiation (2021).
6. M. Tanaka et al., *Enantiomer* **7** 185 (2002).
7. F. Kaneko et al., *J. Phys. Soc. Jpn.* **78** 013001 (2009).

Impacts of Lipid Membranes on Biopolymers' Structuration

Mohamed I. A. Ibrahim[a,b*], Mahmoud E. Esmael[c], Koichi Matsuo[a], Abdelrahman M. Khattab[d]

[a]*Hiroshima Synchrotron Radiation Center, Hiroshima University, 2-313 Kagamiyama, Higashi-Hiroshima, Hiroshima 739-0046, Japan.*
[b]*National Institute of Oceanography and Fisheries (NIOF), Cairo, Egypt.*
[c]*Al-Azhar Center for Fermentation Biotechnology and Applied Microbiology, Al-Azhar University, Nasr City, Cairo 11884, Egypt.*
[d]*Botany and Microbiology Department, Faculty of Science, Al-Azhar University, Nasr City, Cairo 11884, Egypt.*

Keywords: Biopolymer; Polyhydroxybutyrate; *Priestia filamentous;*Circular Dichroism.

Conventional plastics are synthetic polymers derived from non-sustainable sources and have been applied in versatile applications. These plastics suffer from non-biodegradability that allowed the accumulation of tons of plastic in the various environments which have negative impacts on the water quality, living habitats, and soil productivity [1]. There has been an urgent need to control plastic pollution by developing a new type of plastics that possess a high degree of sustainability of being biodegradable and eco-friendly [2]. Polyhydroxyalkanoates (PHAs) have potentially been used for countless purposes in the medical, agriculture, and industrial sectors [3]. They can be biosynthesized by more than 300 microbial species such as bacteria, fungi, and algae [4].

This research presents a sustainable PHA production strategy using a cost-effective microbial isolate, besides the PHA-lipid interactions by circular dichroism (CD) spectroscopy. About 48 bacterial isolates were obtained from multifarious Egyptian sites and screened for PHAs production. The Fe(AZU-A6) was the most potent isolate, and identified genetically as *Priestia filamentosa* AZU-A6. Sugarcane molasses (SCM) was used a cheap carbon source and the production conditions were optimized through a Factor-By-Factor strategy and a Plackett-Burman statistical model. The highest production rate of 6.84 g/L was achieved at 8.0 % SCM, pH 8.0, 35 ◦C, 250 rpm, and 0.5 g/L ammonium chloride after 72 h. Different physicochemical techniques (*e.g.*, FTIR, NMR, GC–MS, DSC, and TGA) have ascertained the structural identity as poly-3-hydroxybutyrate (P3HB) with a characteristic melting temperature of 174.5 ◦C (Data not shown).

Circular dichroism spectroscopy is a well-established technique for investigation the conformation adopted by biomolecules (*e.g.*, nucleic acids, peptides, proteins, carbohydrates, *etc*.) [5]. The structural characteristics of the P3HB using SRCD as well as the changes accompanied the mixing of the PHB with four lipid membranes (DOPE, DOPC, DOPS, and DMPC) at different weight ratios were studied. The structural variations of the P3HB accompanied by the mixing with lipid membranes at different ratios were inspected through the changes in the CD spectra between 200 to 240 nm associated with the $n \rightarrow \pi^*$ transition of ester group in PHB. The CD data showed a broad positive cotton band of a maximum at λ ~ 217.25 nm correspond to the ester group of the polyhydroxy butyrate. The amount of decrement in the CD intensity of PHB demonstrated the order DMPC>DOPE>DOPS>DOPC at 1:1 ratio of L/P (Figure 1), suggesting the highest interaction between DMPC and PHB that induced the largest decrement in the CD intensity up to ~ 82%.

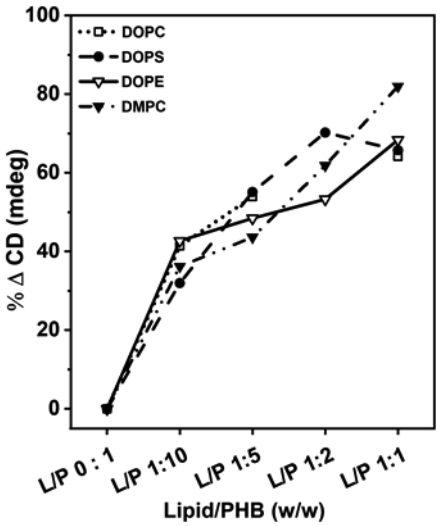

FIGURE 1. Influences of the different lipid molecules on the PHB structuration (Data analyzed based on the VUV-CD spectra of EPS-AG7).

REFERENCES

1. V. Angra, R. Sehgal, and R. Gupta, Microbial Ecology, 2022.
2. N.G. El Menofy and A.M. Khattab, *Plastics Biodegradation and Biofragmentation*, in *Handbook of Biodegradable Materials*. 2022, Cham: Springer International Publishing. p. 1-30.
3. B. Tyagi, et al., Environmental Technology & Innovation, 2021. **24**: p. 101854.
4. M.E. Grigore, et al., Journal of Biomaterials Science, Polymer Edition, 2019. **30**(9): p. 695-712.
5. K. Matsuo and K. Gekko, Methods Mol Biol, 2013. **974**: p. 151-76.

Soft X-ray Polarization Measurements of Phospholipid Multilayers Supported on Hydrophilic Si Surfaces

Masataka Tabuse[a], Akinobu Niozu[a], and Shin-ichi Wada[a,b]

[a]*Graduate School of Advanced Science and Engineering, Hiroshima University*
[b]*Hiroshima Synchrotron Radiation Center, Hiroshima University*

Keywords: Linear Polarization, XAS (X-ray absorption spectroscopy), NEXAFS (near edge X-ray absorption fine structure), Phospholipids, DCCP, DOPC.

Lipid membranes supported on substrates are promising systems for use in biological sensing, biocompatibility, bioelectronics [1]. The idea that ordered lipid molecules can be prepared by several convenient methods, like freeze-thaw and spin-coating methods [2]. We also confirmed that the phospholipid multilayers made by simple dripping of acetone solution onto hydrophilic Si substrates under atmospheric pressure and moisture and room temperature conditions forms well-ordered multilamellar structures. But the quality of ordering as well as formation process of ordered lamellar structure during such a short period is not well understood.

X-ray absorption spectroscopy (XAS) is one of powerful tools to investigate local structural and dynamical information because of its element selectivity. Especially, one can easily get orientation structure around X-ray absorption center by using linearly polarized X-ray beam. In this study, polarization dependence of XAS measured for phospholipid multilayers supported on hydrophilic Si surfaces was investigated in order to quantify the orientation quality.

Measurements of near edge X-ray absorption fine structure (NEXAFS) have been performed at BL-13 of HiSOR, where is a soft X-ray beamline with a Dragon-type spherical grating monochromator developed to investigate soft X-ray spectroscopy for surface organic materials. During measurements, the experimental chamber had a base pressure less than 1×10^{-9} Torr. NEXAFS spectra around the C K-edge were recorded in total electron yield (TEY) mode by measuring a sample drain current by changing incident angle of synchrotron radiation. Polarization at BL-13 is horizontal due to bremsstrahlung from a bending magnet and the polarization factor P was determined to be 0.95 [3] by measuring azimuthal angle-dependent NEXAFS spectra of a highly oriented pyrolytic graphite (HOPG) [4].

DPPC and DOPC phospholipid molecules were used to form supported lipid membranes from 10 to 1000 multilayer by changing the dripping volume of lipid solution onto hydrophilic Si substrates, and moreover for getting the bilayer membranes, multilayers on substrates were considerably washed by immersing Milli-Q water. DPPC and DOPC molecules are shown in Fig. 1, consisting of a polar zwitterionic hydrophilic group and two non-polar carbon chains. So, molecules in aqueous solution form bilayers with the carbon chains facing each other due to hydrophobic interaction. It is understood that bilayers of DPPC with saturated carbon chains form crystalline-like gel phase at room temperature, while DOPC with unsaturated chains composes liquid crystalline phase. Fig. 2 shows typical polarization dependent NEXAFS spectra measured for (a) DPPC and (b) DOPC on Si surfaces at C K-edge. Although DPPC shows clear polarization dependence, the dependence of DOPC in not so dominant. Tendency of such polarization dependence does not depend on the layer number of lipids. So, the different degree of

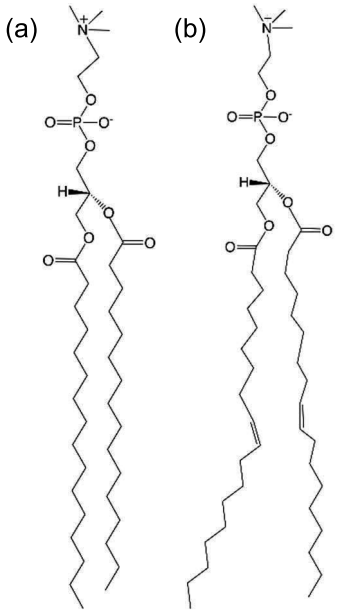

FIGURE 1. Molecular structures of phospholipids (a) DPPC and (b) DOPC.

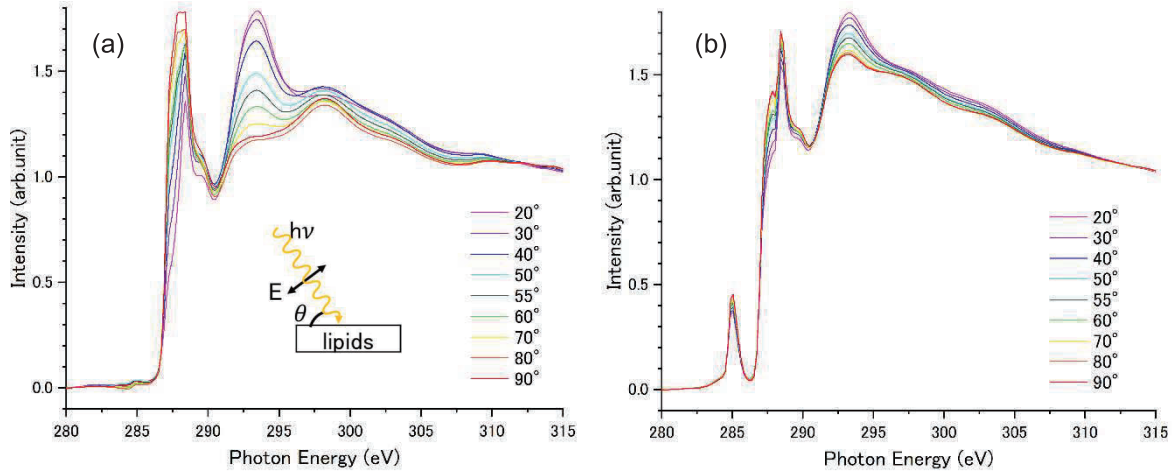

FIGURE 2. Polarization dependent NEXAFS spectra of (a) DPPC and (b) DOPC phospholipids multilamellar membranes measured at C K-edge. These membranes consist of about 100 bilayers, which are confirmed by simple molar consideration and interference of reflected visible light. Incident angle θ from the surface, and therefore the angle of electric vector from the surface normal, is defined like inset.

polarization dependence reflects not only the orientation angles themselves but also the different phase (ordering quality) of lipid membranes. On the basis of above consideration and the careful analysis of polarization dependence of each resonant peaks, DPPC bilayers (that is gel phase) consist of 60% ordered component and 40% non-ordered one, while DOPC bilayers (liquid phase) contain 80% non-ordered carbon chains. This is the first quantitative analysis of phospholipid bilayers of DPPC and DOPC by means of strong advantage of polarization quality and element selectivity of soft-X ray synchrotron radiation.

REFERENCES

1. Z.Zhi, I.Y. Hasan, A. Mechler, *Biotechnol. J.* **13**, 1800101 (2018).
2. A.C. Simonsen and L.A. Bagatolli, *Langmuir* **20**, 9720-9728 (2004).
3. M. Tabuse, K. Yamamoto, S. Wada, *HiSOR Activity Report 2019*, 124 (2020).
4. B. Watts, L. Thomsen and P.C. Dastoor, *J. Electron Spectrosc. Relat. Phenom.* 151, 208 (2006).

Characterization of self-assembled monolayers of methyl-ester terminated naphthalenethiol

A. Niozu[a], H. Sunohara[b], S. Tendo[a], M. Tabuse[a], and Shin-ichi Wada[a,c]

[a]*Graduate school of advanced science and engineering, Hiroshima University, Higashi-Hiroshima 739-8526, Japan*
[b] *Faculty of science, Hiroshima University, Higashi-Hiroshima 739-8526, Japan*
[c]*Hiroshima Synchrotron Radiation Center, Hiroshima University, Higashi-Hiroshima 739-0046, Japan*

Keywords: Self-assembled monolayers (SAMs), Near edge X-ray absorption fine structure (NEXAFS)

Core-electron excitations by soft X-ray radiation possess several unique properties that differ from those of valence excitations. Core-excitation energy depends on the element and its chemical environment, which allows selective excitation of a specific atom in a molecule. In general, core excitation is followed by Auger decay on a time scale of a few femtoseconds, resulting in final states with large excess energy. Thereafter, the excited molecule follows a rich variety of relaxation pathways, e.g. desorption of ion and neutral species and charge transfer within the molecule.

An interesting phenomenon that reflects the selective nature of core excitation is site-selective bond breaking of molecules, i.e. the so-called “molecular scalpel” [1,2]. In particular, it has been reported that highly site-selective bond scission can be achieved in self-assembled monolayers (SAMs) of molecules absorbed on metal surfaces [1,2]. Furthermore, our recent experiments on aliphatic and aromatic SAMs have suggested that the degree of site-selective bond scission depends on the molecular structure of backbone between the excitation cite and the metal substrate. This implies the key role of energy transfer between the excitation cite and the substrate for the manifestation of site-selective bond scission. To corroborate this picture, a systematic experimental study about the fragmentation dynamics dependent on the molecular structure is helpful.

In this study, we investigated the ion desorption dynamics of SAMs of methyl-ester terminated naphthalenethiol molecules. The SAM samples were prepared by immersing Au substrates in 1.0 mM benzene solution of the sample molecules for 24 hs. We characterized the prepared SAM samples by near-edge X-ray absorption fine structure (NEXAFS) measurements. The experiment was performed at the BL 13 of HiSOR. The C K-edge NEXAFS spectra were measured by the total electron yield (TEY) method via the sample drain current. The measurements were performed at different incident beam angles, and polarization dependence of the NEXAFS intensity was investigated. The obtained NEXAFS spectra (Fig. 1) show peaks corresponding to excitations to individual unoccupied molecular orbitals and provided precise values of their excitation energies. In addition, the spectra exhibit a clear polarization dependence, which supports the formation of well-oriented SAMs on the substrate.

The measurements of desorbed ions were performed at BL 2B of photon factory (PF) in KEK. PF was operated in the hybrid operation mode, and the single-bunch component of the X-ray beam was skimmed and used in the experiment. Partial ion yield (PIY) spectra were recorded with a time-of-flight ion spectrometer. The PIY of CH_n^+ (n=0,1,2,3) ions showed a prominent enhancement at the C1s(OCH_3)→ σ^*(O-CH_3) resonant excitation, which have been observed in previous experiments on methyl-ester terminated SAMs [1,2]. From the PIY spectra, we evaluated the degree of site-selective desorption by analyzing the relative yield of CH_n^+ ions. The degree of site-selectivity for the present molecule with naphthalene backbone was evaluated to be between those for molecules with benzene and biphenyl (with two benzene rings) backbones. The present results corroborate the correlation between the molecular conductivity and the site selectivity in ion desorption.

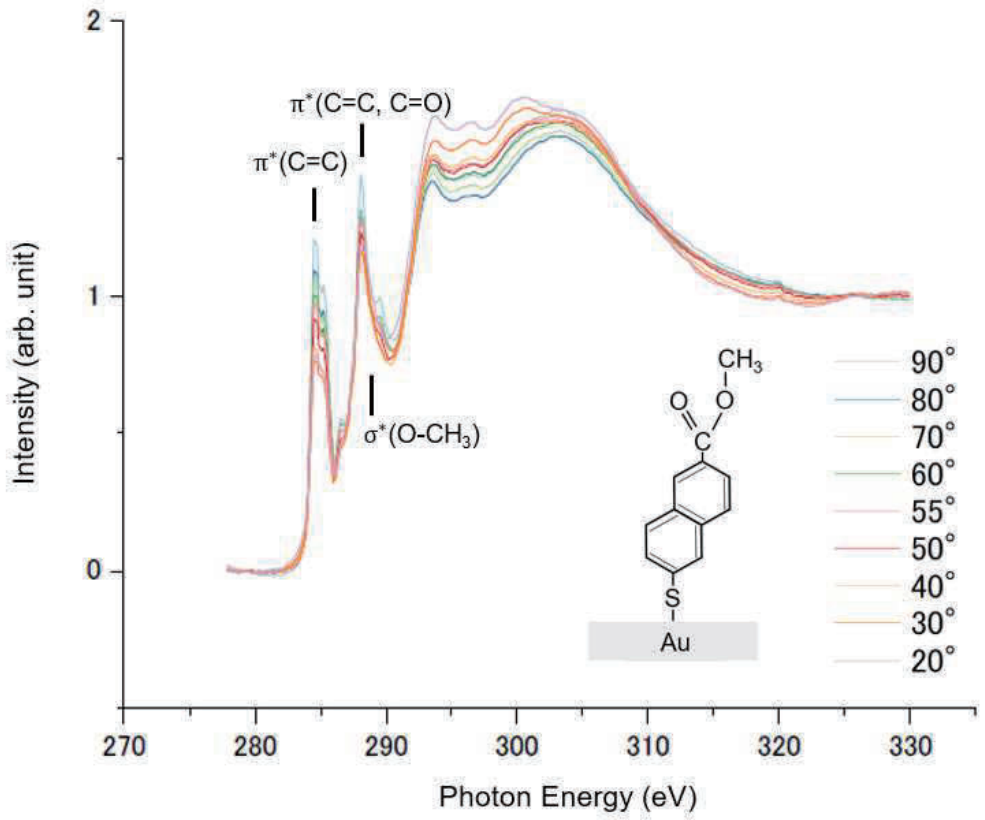

FIGURE 1. TEY spectra for methyl-ester terminated naphthalenethiol SAMs. The spectra exhibit peaks corresponding to excitations to individual π^* and σ^* orbitals. The spectra show a clear polarization dependence, which supports the formation of ordered SAMs on the Au substrate.

REFERENCES

1. S. Wada, H. Kizaki, Y. Matsumoto, R. Sumii, and K. Tanaka, J. Phys. Condens. Matter **18**, 1 (2006).
2. S. Wada, and K.Tanaka, J. Mass Spectrom. Soc. Jpn **58**, 17 (2010).

C K-edge XAFS measurements for detection of unsaturated bonds in organically bridged silica materials

Shinjiro Hayakawa [a], Joji Oshita[a,b], Kei Oshima[a,b], Shogo Tendo[c],

Toshinori Tsuru[d], Shinichi Wada[c]

a *Applied Chemistry program, Graduate School of Applied Science and Engineering,, Hiroshima University, Higashi-Hiroshima, Hiroshima 739-8527, Japan*
b *Smart Innovation program, Graduate School of Applied Science and Engineering,, Hiroshima University, Higashi-Hiroshima, Hiroshima 739-8527, Japan*
c *Physics program, Graduate School of Applied Science and Engineering,, Hiroshima University, Higashi-Hiroshima, Hiroshima 739-8526, Japan*
d *Chemical Engineering program, Graduate School of Applied Science and Engineering,, Hiroshima University, Higashi-Hiroshima, Hiroshima 739-8527, Japan*

Keywords: XAFS, unsaturated bond, organosilica, carbon K-edge

Introduction

Microporous organosilica membranes are attractive because of unique features such as a high surface area, improved hydrothermal stabilities, and applications of them are widely expanding [1]. Most of researches have been focused on bis-(triethoxysilyl)ethane (BTESE) and characteristics of BTESE derived materials. To expand the possibilities of organosilica membranes we have been exploring different precursors to introduce ethylene and acetylene bridges into the organosilica membranes. Though the properties of the synthesized organosilica were characterized by the many analytical methods, there exists no method that provide the evidence of the unsaturated carbon bond. Moreover, the quantification of the amount of the unsaturated bonds is quite difficult. We have utilized C K-edge XAFS spectroscopy for detecting remained unsaturated bonds in PMOs, and the possibilities of quantification will be discussed.

2. Experimental

2.1 Samples

Table 1 shows precursors used for synthesis of organically bridged silica materials. Three types of precursor were utilized including bis-(triethoxysilyl)ethane, bis-(triethoxysilyl)ethylene and bis-(triethoxysilyl)acetylene, and their ethoxysil groups were converted into siloxane or silanor groups via the hydrolysis and polymerization. Ethanol solutions of samples (5 wt %) were prepared for each, and a 30 μL of the solution was dropped three times onto a Si substrate of approximately 15 mm square under atmospheric condition.

TABLE 1. Samples and their precursors of the organically bridged silica materials investigated.

Sample name	Precursor	Approximate mass fraction of carbon
BTES-E1 ethane bridge	$(EtO)_3SiCH_2CH_2Si(OEt)_3$	18.17 %
BTES-E2 ethylene bridge	$(EtO)_3SiCHCHSi(OEt)_3$	18.45 %
BTES -E3 acetylene bridge	$(EtO)_3SiCCSi(OEt)_3$	18.74 %

2.2 XAFS measurements

Experiments were carried out on the beamline BL13 [2]. Incident X-rays were monochromatized with a grating monochromator, and the incident X-ray intensity was monitored from a Au coated grid of stainless steel. The beam size at the sample position was approximately 1 mm square, and the glancing angle of 20 deg. was employed for X-ray absorption fine structure (XAFS) measurements. Total electron yield (TEY) from a sample was monitored, and the normalized spectra were utilized for the further analysis. To avoid the inhomogeneity of the sample on the substrate, several positions on the sample were selected for measurements. Incident X-ray energy was calibrated with the main peak obtained with PMMA, and the observed spectra were shifted to 1.44 eV minus to let the peak energy of PMMA be 288.34 eV.

3. Results and discussion

Figure 1 shows C K-edge XAFS spectra of organically bridged silica materials. Obtained main peak with ethane bridged silica material (BTES-E1) showed a main peak around 290.2 eV, and the spectrum was almost identical to that obtained with the blank (Si substrate). On the other hand two spectra of ethylene bridged silica material (BTES-E2) showed the characteristic peak around 285.04 eV. The peak energy was similar to the reported value of 1s to π* transition (around 285 eV) obtained from the adsorbed ethylene on the Si substrate [3]. Though the similar peak corresponding to1s to π* transition was expected with acetylene bridged silica, no clear peak was observed while the broadened peaks remained in the present experiment. It was clear that the direct evidence of the remaining unsaturated carbon bond in the organically bridged silica material could be monitored with the C K-edge XAFS spectroscopy. While the contribution of the surface contamination with the hydrocarbon should be considered for determination of the portion of the unsaturated bond in the sample.

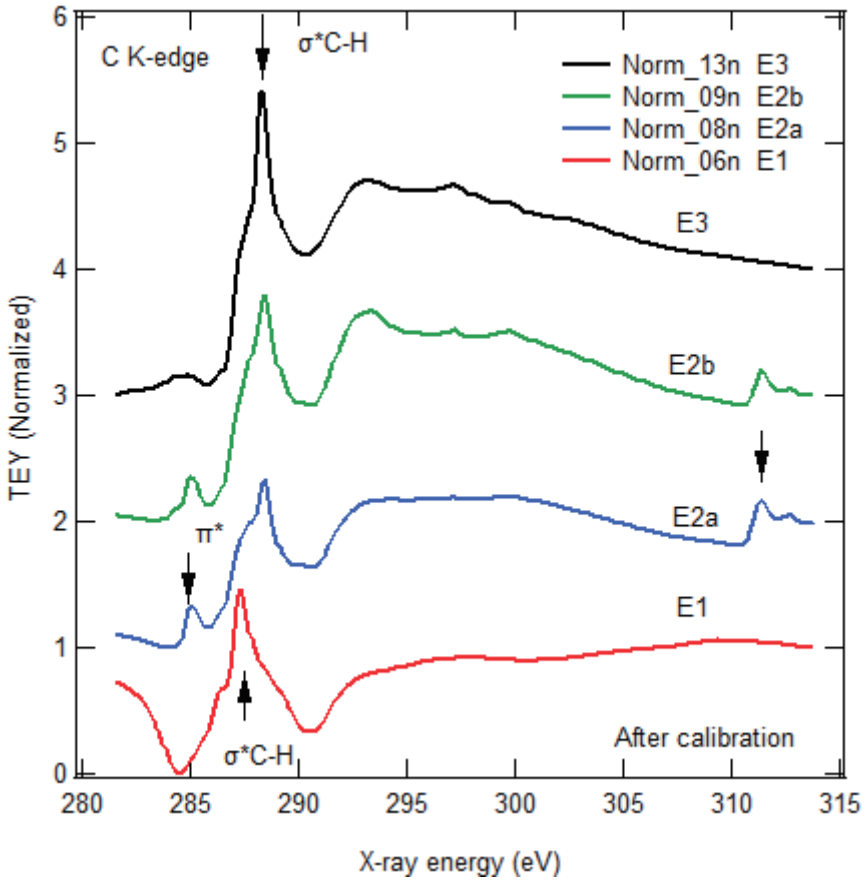

REFERENCES

1. R. Xuet al., Appl. Mater. Interfaces 6(2014) 9357-9364.
2. S. Wada et al., Surf. Sci. 601 (2007) 3833-3837.
3. F. Matsui et al., Surf. Sci. 401 (1998) L413-419.

NEXAFS Study of Fullerene Adsorbed on Aminothiophenol Self-Assembled Monolayer

K. Kono[a] , S. Wada[b,c] and T. Sekitani[b,c]

[a]*Faculty of Science, Hiroshima University*
[b]*Graduate School of Advanced Science and Engineering, Hiroshima University*
[c]*Hiroshima Synchrotron Radiation Center, Hiroshima University*

Keywords: fullerene, self-assembled monolayer, NEXAFS

Controlling the microstructure of organic materials to nanometer scale has motivated scientific studies of molecular structure and molecular interactions on various surfaces. Among the various techniques for the preparation of ordered thin organic films, the self-assembled films provide the desired control of molecular order at the interface and also introduce various functional groups into the molecular systems with a high degree of control over the orientation of those groups. The adsorption of thiols onto gold surfaces has attracted considerable interest, as it has been shown that such adsorption can result in formation of well-organized self-assembled monolayer (SAM) [1]. The organothiol self-assembly on metal surface have attracted much interest in a facile manipulating of surface functionality. The SAM have successfully employed as components in molecular electronic devices. Self-assembly of aromatic thiols are particularly interesting due to the interaction of delocalized π orbital of phenyl ring.

The unique electronic, spectroscopic, and structural properties of fullerene and fullerene derivative are very useful to the various application of the material. C_{60} is characterized by the delocalized and highly degenerate orbitals due to π bonding and I_h symmetry. C_{60} is also served as an excellent electron acceptor in molecularly designed donor-acceptor systems, such as molecular photovoltaics [2]. Attachment of C_{60} to the tail groups of SAM provides discrete monolayers of C_{60} and also organized assembly where C_{60} will remain immobilized on the surface.

In this study, the adsorbed state of C_{60} on SAM was examined by NEXAFS spectroscopy. 4-aminothiophenol was used as SAM. The aminothiophenol SAM was prepared by immersing the gold coated Si substrate to 1 mM solution in ethanol for 24 h. The aminothiophenol SAM was cleaned with ethanol and dipped further in 1 mM C_{60} solution in benzene and kept for 24 h. The SAMs thus formed were washed with benzene, ethanol, and dichloromethane. C_{60} multilayer was formed by dropping benzene solution to gold coated substrate and drying in air. NEXAFS measurements were performed at BL13 of Hiroshima Synchrotron Radiation Center.

C K-edge NEXAFS spectra were measured for $C_{60,}$ aminothiophenol SAM and C_{60} adsorbed aminothiophenol SAM. Since NEXAFS spectrum of C_{60} adsorbed SAM includes contribution of aminothiophenol, the component of C_{60} in the C_{60}-SAM was obtained by subtraction of aminothiophenol SAM spectrum from C_{60}-SAM spectrum. The obtained difference spectrum shows similar feature as C_{60} spectrum, but shows peak shifts and peak broadening compared with C_{60} spectrum. Particularly, LUMO peak is shifted to higher photon energy and overlapped with LUMO+1 peak. A higher photon energy shift of LUMO is observed at C_{60} adsorbed on 11-amino-1-undecane thiol SAM [3]. The results suggest that C_{60} is chemisorbed on amino thiolate SAM by hybridization between N Pz of amino group and π* orbital of C_{60}.

REFERENCES

1. J. C. Love, L. A. Estroff, J. K. Kriebel, R. G. Nuzzo, G. M. Whitesides, *Chem. Rev*. **105**, 1103 (2005)
2. H.Imahori, Y.Kashiwagi, T. Hasebe, M. Kimura, T. Hanada, Y. Nishimura, I. Yamazaki, Y. Araki, O. Ito, S. Fukuzumi, *Thin Solid Films*. **451-452**, 580 (2004)
3. A.Patnaik, K.Okudaira, S.Kera, H.Setoyama, K.Mase, N.Ueno, *J. Chem. Phys*. **122**, 154703 (2005)

XAS study of spin-state related percolative dynamics in magnetic cobaltites

Meng Wang [a]

[a]*RIKEN Center for Emergent Matter Science (CEMS), Wako 351-0198, Japan*

Mixed-valent cobaltite is a double-exchange ferromagnetic system, as analogous to the double-exchange manganite. However, the colossal magnetoresistance (CMR) associated with a magnetic-field-driven insulator-metal transition (IMT) at the phase boundary has not yet been reported in cobaltite. Combining magnetic transport, magnetization, magnetic-force-microscopy (MFM), and X-ray absorption spectroscopy (XAS) measurements, we conducted a systematic research on the $La_{0.7}AE_{0.3}CoO_3$ (AE = Ca, Sr, and Ba) films and unveiled the hidden mechanisms that dominate the phase transition dynamics in cobaltite. First, in contrast to utilizing the bulk crystal, we fabricated films on a $SrTiO_3$ substrate with tensile strain to drive it to the insulator-metal phase boundary. All films exhibit a ferromagnetic and non-ferromagnetic phase separation, which is robust against an isothermal magnetic field sweeping, while a percolation induced insulator-to-metal transition can be achieved by a field-cooling process. Such a thermodynamic-history-dependent properties signify a nonergodic feature associated with the dynamics of magnetic domains. By further comparing the nonergodic properties and the spin-sates among $La_{0.7}AE_{0.3}CoO_3$ films by the transport and XAS measurements, respectively, we reveal that the mixed low-spin Co^{3+} forms a key factor to enhance the energy barrier for domain-wall motions during domain percolation. Such a spin-state degree of freedom is absent in manganites, probably resulting in the large difference of the phase evolution kinetics in the magnetic-field-induced IMT between cobaltite and manganite. [1]

REFERENCES

1. M. Wang,† K. Matsuura, M. Nakamura, M. Sawada, M. Kawasaki, and F. Kagawa, “Magnetic field control of insulator-metal crossover in cobaltite films via thermally activated percolation”. *Phy. Rev. B* **106**, 155135 (2022).

Characterization of amorphous carbon films by X-ray magnetic circular dichroism

Yuji Muraoka[a], Taishi Kanayama[a], Sho Enomoto[a], Takanori Wakita[a], and Masahiro Sawada[b]

[a]*Research Institute for Interdisciplinary Science, Okayama University, Japan*
[b]*Hiroshima Synchrotron Radiation Center, Hiroshima University, Japan*

Keywords: Amorphous carbon, sp^3, Pulsed laser annealing, XAS

Upon pulsed laser annealing (PLA) with a laser energy density above threshold value, amorphous carbon films are melted and then transformed into allotropes such as Q-carbon, nanodiamond, and reduced graphene oxide, depending on the quench rate during liquid-phase regrowth [1, 2]. Q-carbon, which was recently discovered, has a high sp^3 contents of about 80% and shows excellent physical properties such as hardness superior to that of diamond, room-temperature ferromagnetism, and even high-temperature superconductivity when boron is doped with Q-carbon. Since it has peculiar physical properties, Q-carbon is of interest in terms of both fundamental and application viewpoints [3].

Q-carbon is prepared by irradiating ArF and KrF excimer lasers to the amorphous carbon films. A challenging study is to prepare the Q-carbon by using a YAG solid-state laser with a wavelength of 355 nm. This is because the wavelength of 355 nm is longer than those of excimer lasers (193 nm for ArF laser and 248 nm for KrF laser) and is close to visible light. The successful preparation of Q-carbon by using the 355 nm YAG laser will help expand the preparation condition and accelerate the research for Q-carbon. In this experiment, the 355 nm YAG laser was applied to the PLA treatment for amorphous carbon films and X-ray absorption and X-ray photoemission spectroscopies were employed for characterization of the obtained films .

Amorphous carbon films were prepared using a YAG laser with a wavelength of 355 nm. The same laser was employed for PLA treatments. X-ray absorption spectroscopy measurements were performed at HiSOR BL14. Photoemission spectroscopy measurements were conducted at Spring-8 BL25 SU. All measurements were performed at room temperature.

Figure 1(a) shows XAS spectra at C *K*-edge for amorphous carbon films before and after PLA. A signal related to the sp^3 state was seen at 290 eV. A decrease in the intensity at 290 eV was observed for the film after PLA, suggesting the reduction of sp^3 contents in the film after PLA. Figure 1 (b) shows the photoemission C 1s core-level spectra of the films before and after PLA. Clearly seen was the decrease in the intensity at 285.3 eV which corresponds to the binding energy of sp^3 states in carbon. The sp^3 content was estimated from the area ratio of the sp^2 and sp^3components to be approximately 40% for the film before PLA and 20% for the film after PLA. The sp^3 content in the film is reduced by PLA, which is consistent with the result of XAS measurements.

The sp^3 content in the films is decreased by PLA. The estimated sp^3 content for the film after PLA is smaller than that of Q-carbon. The results show that the quenching rate required for Q carbon formation is insufficient, and suggest that a higher quench speed is needed for obtaining the Q-carbon. Laser energy density for PLA and/or film thickness are effective experimental parameters to improve the quench speed. We believe that Q carbon can be prepared using a YAG laser with a 355 nm wavelength by optimizing experimental conditions.

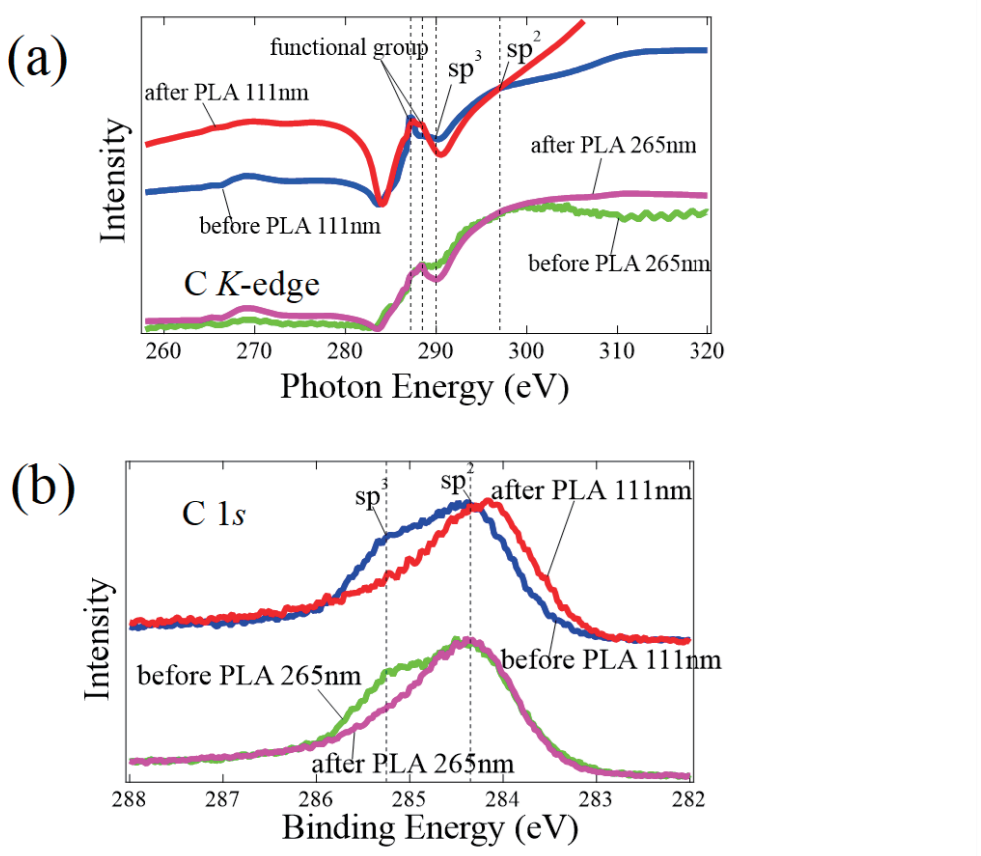

FIGURE 1. (a) XAS spectra at C *K*-edge for amorphous carbon films before and after PLA. The spectral intensity is normalized at 298 eV which corresponds to the signal related to the sp^2 states. (b) Photoemission spectra of C 1s core-level for amorphous carbon films before and after PLA. Photon energy of 1330 eV was used for measurements.

REFERENCES

1. S. Gupta *et al., Appl. Nano Mater.* **3**, 5178 (2020).
2. S. Gupta *et al., JOM.* **70**, 450 (2018).
3. J. Narayan, and A. Bhaumik, *J. Appl. Phys.* **118**, 215303 (2015).

XMCD study of magnetic thin-films of FeMn alloys grown on h-BN/Ni(111)

Wataru Nishizawa[a] and Masahiro Sawada[b]

[a]*Graduate School of Science, Hiroshima University*
[b]*Hiroshima Synchrotron Radiation Center, Hiroshima University*

Keywords: XMCD, ultrathin films, hexagonal boron nitride, FeMn alloys

Magnetic tunneling junction (MTJ) structures, where ferromagnetic electrode layers sandwich an insulating barrier layer, show tunnel magnetic resistance (TMR) effect that is widely applied for spintronics devices such as magnetic random-access memory. One of important performance factors of TMR element is magnetic resistance (MR) ratio, which is sensitive to both of interfacial structure and magnetic state. Conventionally, metal oxide layers have been utilized for the barrier layer in the device structures. However, further improvement of MR ratio is difficult in MTJ with such oxide-based barriers, because of crystal disorder arises from lattice mismatch and defect formation at the interface. In recent years, much attention and intensive studies have been devoted to hexagonal boron nitride (h-BN) whose structure is two-dimensional honeycomb formed by stable chemical bonding. Monolayer h-BN is one of good candidates for the ideal burrier layer of TMR devices because the h-BN layer is expected to form a pinhole-less and flat interface with magnetic layers. Recently, in Fe or Co layers grown on the monolayer h-BN uniformly established on a single crystal substrate of Ni(111), anti-ferromagnetic coupling has been found between the overlayer and Ni substrate. An effect of electron filling control in the 3d valence band of the overlayer is of great interest, to investigate the origin of unexpected magnetic coupling through the h-BN monolayer.

In this study, we have investigated interlayer magnetic coupling between the FeMn films and the Ni substrate by means of XMCD spectroscopy at $L_{2,3}$ absorption edges of Fe, Mn and Ni. Ultrathin films of FeMn alloys were fabricated on h-BN/Ni(111) in ultra-high vacuum condition, whose XMCD spectra were measured *in-situ*. In Fig.1(a) and (b), XAS spectra for $Fe_{84}Mn_{16}$/h-BN/Ni(11) are shown at Ni and Fe $L_{2,3}$ edge, respectively. The red (blue) curves are corresponding to excitation light with helicity parallel(antiparallel) to external magnetic field of 1.1 T along to the sample normal direction. XMCD signals of Ni and Fe are opposite each other at both L_2 and L_3 edge. That means anti-ferromagnetic coupling through h-BN monolayer. Overlayer thickness dependence of XMCD for the $Fe_{84}Mn_{16}$/h-BN/Ni(111) sample (shown in Fig.1(c)) indicates gradual change of magnetization direction from antiparallel into parallel to the applied magnetic field, with the thickness increasing. The critical thickness where the sign of XMCD recovers into positive, includes information on energetic stability of interlayer magnetic coupling. The concentration dependence of the critical thickness has also been found in our series of XMCD experiments for the alloy films with different concentration of Fe and Mn.

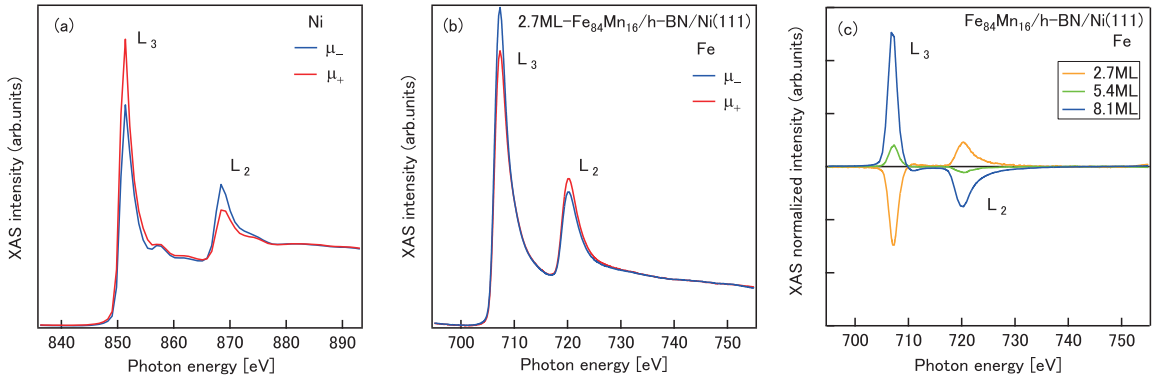

FIGURE 1. XAS spectra for (a) Ni substrate and (b) Fe atomic site in the FeMn alloy layer whose concentration of Fe is 84%. (c) Thickness dependence of the XMCD signals ($\mu_+ - \mu_-$) of Fe in the FeMn film on h-BN/Ni(111).